BNL-71205-2003-CP

THE TOP QUARK, QCD, AND NEW PHYSICS

S. DAWSON*
Physics Department, Brookhaven National Laboratory,
Upton, NY 11973, USA
dawson@bnl.gov

The role of the top quark in completing the Standard Model quark sector is reviewed, along with a discussion of production, decay, and theoretical restrictions on the top quark properties. Particular attention is paid to the top quark as a laboratory for perturbative QCD. As examples of the relevance of QCD corrections in the top quark sector, the calculation of $e^+e^- \to t\bar{t}$ at next- to-leading-order QCD using the phase space slicing algorithm and the implications of a precision measurement of the top quark mass are discussed in detail. The associated production of a $t\bar{t}$ pair and a Higgs boson in either e^+e^- or hadronic collisions is presented at next-to-leading-order QCD and its importance for a measurement of the top quark Yukawa coupling emphasized. Implications of the heavy top quark mass for model builders are briefly examined, with the minimal supersymmetric Standard Model and topcolor discussed as specific examples.

1. Introduction

Long before its discovery in 1995,[1] the top quark was regarded as an essential ingredient of the Standard Model (SM) of particle physics. Its existence, and many of its properties, are determined by requiring the consistency of the Standard Model. These requirements (discussed in Section 2) specify the couplings of the top quark to the $SU(3) \times SU(2)_L \times U(1)_Y$ gauge bosons and many of the top quark properties:

- $Q^t_{em} = \frac{2}{3} \mid e \mid$
- Weak isospin partner of b quark: $T^t_3 = \frac{1}{2}$
- Color triplet
- spin-$\frac{1}{2}$

*This work is supported by the U.S. Department of Energy under contract number DE-AC02-76-CH-00016.

The top quark mass, which is measured at CDF and D0 to be $M_t = 174.3 \pm 5.1\ GeV$,[2] is not predicted in the Standard Model, but is restricted by precision electroweak measurements.[3,4] In order to confirm that the observed top quark is that predicted by the Standard Model, all of the properties listed above must be experimentally verified by direct observation. Section 3 contains a discussion of the measurements of top quark properties at the Tevatron and surveys the improvements expected at future colliders. Recent reviews of top quark physics can be found in Ref. 5.

In Section 4, we discuss the top quark as a laboratory for perturbative QCD. At the top quark mass scale, the strong coupling constant is small, $\alpha_s(M_t) \sim 0.1$, and so QCD effects involving the top quark are well behaved and we expect a perturbation series in α_s to converge rapidly. The process $e^+e^- \to t\bar{t}$ provides an example of QCD effects in top quark production and the next-to-leading-order (NLO) QCD corrections are described in detail using the phase space slicing (PSS) algorithm. A knowledge of these higher order QCD corrections is vital for extracting a precise value of the top quark mass from the threshold behavior of the $e^+e^- \to t\bar{t}$ cross section. As a further example of the role of QCD effects in the top quark sector, we consider the associated production of $t\bar{t}h$ and the implications for measuring the top quark Yukawa coupling.

Finally, in Section 5, we discuss the importance of the top quark mass in model building. Since the top quark is heavy, it is expected to play a special role in elucidating the source of fermion masses. We begin by discussing the significance of the top quark in supersymmetric models, and finish with a brief discussion of the top quark and models with dynamical symmetry breaking.

2. Who needs a top quark?

In this section we discuss some of the reasons why the top quark was believed to exist even before its experimental discovery. These considerations fall into three general categories: theoretical consistency of the Standard Model gauge theory (anomaly cancellation), consistency of b quark measurements with SM predictions, and consistency of precision measurements with the SM. We then turn to a discussion of top quark production and decay mechanisms at the Tevatron and the LHC.

The particles of the first generation of fermions, along with the Higgs doublet, are shown in Table 1, with their gauge quantum numbers. The third generation is assumed to follow the same pattern, with the left-handed

top and bottom quarks forming an $SU(2)_L$ doublet with hypercharge, $Y = \frac{1}{6}$. The right-handed top and bottom quarks are $SU(2)_L$ singlets. Our normalization is such that:

$$Q_{em} = T_3 + Y \tag{1}$$

with $T_3 = \pm\frac{1}{2}$.

Table 1. Fermions in the first generation of the Standard Model and their $SU(3) \times SU(2)_L \times U(1)_Y$ quantum numbers.

Field	$SU(3)$	$SU(2)_L$	$U(1)_Y$
(u_L, d_L)	3	2	$\frac{1}{6}$
u_R,	3	1	$\frac{2}{3}$
d_R,	3	1	$-\frac{1}{3}$
(ν_L, e_L)	1	2	$-\frac{1}{2}$
e_R	1	1	-1
H	1	2	$\frac{1}{2}$

2.1. *Anomaly Cancellation*

The requirement of gauge anomaly cancellation[6,7] puts restrictions on the couplings of the fermions to vector and axial gauge bosons, denoted here by V^μ and A^μ. The fermions of the Standard Model have couplings to the gauge bosons of the general form:

$$L \sim g_A \overline{\psi} T^\alpha \gamma_\mu \gamma_5 \psi A^{\alpha\mu} + g_V \overline{\psi} T^\alpha \gamma_\mu \psi V^{\alpha\mu}, \tag{2}$$

where T^α is the gauge generator in the adjunct representation. These fermion-gauge boson couplings contribute to triangle graphs of the form shown in Fig. 1. The triangle graphs diverge at high energy,

$$T^{abc} \sim Tr[\eta_i T^a \{T^b, T^c\}] \int \frac{d^n k}{(2\pi)^n} \frac{1}{k^3}, \tag{3}$$

where $\eta_i = \mp 1$ for left- and right-handed fermions, $\psi_{L,R} = \frac{1}{2}(1 \mp \gamma_5)\psi$. This divergence is independent of the fermion mass and depends only on the fermion couplings to the gauge bosons. Such divergences cannot exist in a physical theory, and must somehow be cancelled. The theory can be anomaly free in a vector-like model where the left- and right-handed particles have identical couplings to gauge bosons and the contribution to

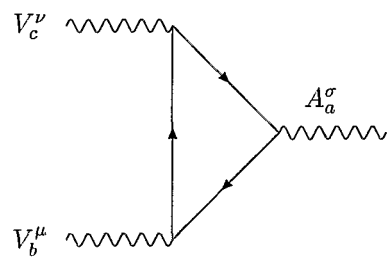

Figure 1. Generic Feynman diagram contributing to gauge anomalies. The fermion loop contains all fermions transforming under the gauge symmetry. a, b, c are gauge indices.

Eq. 3 cancels for each pair of particles. From Table 1, however, it is clear that the Standard Model is not vector-like. The anomaly, T^{abc}, must therefore be cancelled by a judicious choice of fermion representations under the various gauge groups.

The only non-vanishing contribution to the anomaly in the Standard Model is from

$$\Sigma Tr[Y\{T^a, T^b\}], \tag{4}$$

where T^a are the $SU(2)_L$ generators and the sum is over all fermions in the theory. Eq. 4 vanishes for the hypercharge assignments given in Table 1. Note that the anomaly cancels separately for each generations of fermions. The cancellation of the gauge anomalies in the Standard Model for the third generation therefore requires that the b quark have a $T_3 = \frac{1}{2}$ partner with electric charge $Q^t_{em} = \frac{2}{3} \mid e \mid$, and hypercharge $Y^t = Q^t_{em} - T^t_3$. The partner of the b quark is by definition the top quark. Since anomaly cancellation is independent of mass, *a priori*, the top quark mass could be anything.

2.2. *b quark properties*

Many of the experimental properties of the b quark require that it be a $T^b_3 = -\frac{1}{2}$ particle with $Q^b_{em} = -\frac{1}{3}$ and $Y^b = \frac{1}{6}$. The coupling of the b quark to the Z boson can be tested to check if it has these quantum numbers. The SM fermions couple to the Z boson as,

$$L = -\frac{g}{4\cos\theta_W}\overline{\psi}\gamma_\mu\Big[R_i(1+\gamma_5) + L_i(1-\gamma_5)\Big]\psi_i Z^\mu \ , \tag{5}$$

where

$$R_i = -2Q_i \sin^2\theta_W$$
$$L_i = 2T_{3i} - 2Q_i \sin^2\theta_W \ , \tag{6}$$

and θ_W is the electroweak mixing angle. The experimental value of R_{had} is sensitive to Q^b_{em},

$$R_{had} \equiv \frac{\sigma(e^+e^- \to \text{hadrons})}{\sigma(e^+e^\to \mu^+\mu^-)} \ . \tag{7}$$

At a center-of-mass energy, $\sqrt{s} = 2m_b$, R_b depends sensitively on the b quark electric charge,

$$\delta R_{had}(2m_b) = N_c(Q_b)^2 + O(\alpha_s), \tag{8}$$

where $N_c = 3$ is the number of colors. The experimental measurement,[8]

$$\delta R_{had}(2m_b) = .36 \pm .09 \pm .03 \tag{9}$$

is in good agreement with the theoretical prediction from $Q^b_{em} = -\frac{1}{3}$, verifying the SM electric charge assignment of the b quark.

Similarly, the $SU(2)_L$ quantum numbers of the left- and right- handed b quarks are probed by the decay rate for Z to $b\bar{b}$ quark pairs. If the b did not have a top quark partner, it would be an isospin 0 particle ($T^b_3 = 0$) and the decay width would be dramatically different from that of the SM. The decay width is given in terms of the left and right- handed couplings of the Z to the $b\bar{b}$ pair,[9]

$$\Gamma(Z \to b\bar{b}) = \frac{G_F M_Z^3}{4\sqrt{2}\pi}(L_b^2 + R_b^2). \tag{10}$$

If the b quark were an isospin singlet, then the decay width would be changed,

$$\frac{\Gamma(Z \to b\bar{b})^{T^b_3 = -\frac{1}{2}}}{\Gamma(Z \to b\bar{b})^{T^b_3 = 0}} = \frac{1 + 4Q_b \sin^2\theta_W + 8Q_b^2 \sin^4\theta_W}{8Q_b^2 \sin^4\theta_W}$$
$$\sim 13 \quad .$$

The measurement of the $Z \to b\bar{b}$ decay width excludes the $T^b_3 = 0$ hypothesis for the b quark.[3]

- The measured b couplings, combined with anomaly cancelation, require that the b quark have a $T^t_3 = \frac{1}{2}$, color triplet, fermion partner: this is the top quark.

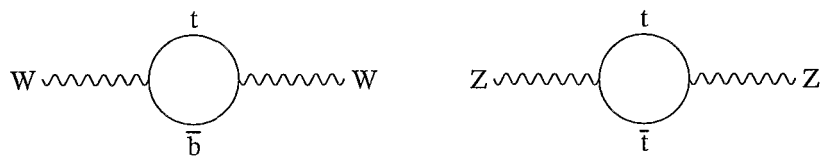

Figure 2. Feynman diagrams for gauge boson self-energies which give contributions proportional to M_t^2.

2.3. *Precision Measurements*

Before the top quark was discovered, an approximate value for its mass was known from precision measurements, which depend sensitively on the top quark mass. At tree level, all electroweak measurements depend on just three parameters: the $SU(2)_L \times U(1)_Y$ gauge coupling constants and the Higgs vacuum expectation value, $v = 246\ GeV$. These are typically traded for the precisely measured quantities, α, G_F, and M_Z. All electroweak measurements at lowest order can be expressed in terms of these three parameters. Beyond the lowest order, electroweak quantities depend on the masses of the top quark and the Higgs boson.

A typical example of the role of the top quark mass in precision measurements is the calculation of the ρ parameter,

$$\begin{aligned} \rho &\equiv \frac{M_W^2}{M_Z^2 \cos^2\theta_W} \\ &= \frac{A_{WW}(0)}{M_W^2} - \frac{A_{ZZ}(0)}{M_Z^2}, \end{aligned} \tag{11}$$

where A_{VV} is defined by the gauge boson 2- point functions,

$$i\Pi_{VV}^{\mu\nu} \equiv A_{VV}(p^2) g^{\mu\nu} + B_{VV} p^\mu p^\nu. \tag{12}$$

At tree level, the ρ parameter in the Standard Model is exactly one, but at one loop it receives contributions from gauge boson, Higgs boson, and fermion loops. The largest corrections are those involving the top quark loop. For simplicity, we compute only the corrections proportional to M_t^2, which are found from the diagrams of Fig. 2.

The 2-point function of the Z boson is given by,

$$i\Pi_{ZZ}^{\mu\nu} = -N_c \left(\frac{-ig}{4c_W}\right)^2 (i)^2 \int \frac{d^n k}{(2\pi)^n} \frac{T^{\mu\nu}}{[den]} \tag{13}$$

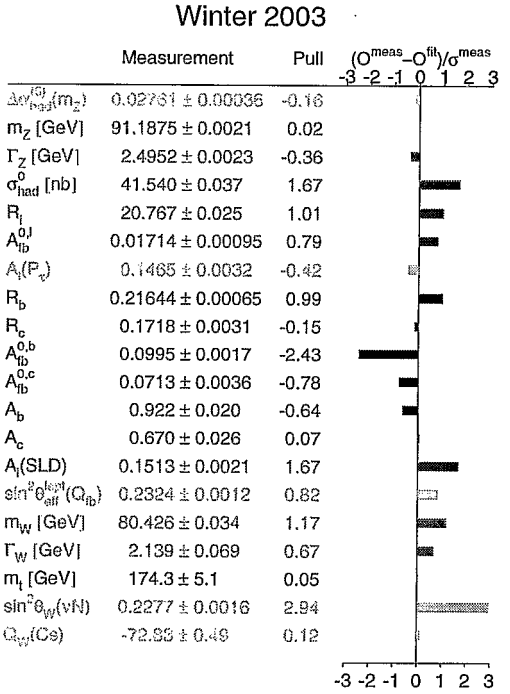

Figure 3. Fits to electroweak data. The bars show the pull from the Standard Model global fit.[3]

where $c_W \equiv \cos\theta_W$ and ,

$$T^{\mu\nu} = Tr[(k + M_t)\gamma^\mu(R_t P_+ + L_t P_-)(k - p + M_t)\gamma^\nu(R_t P_+ + L_t P_-)]$$
$$den = [k^2 - M_t^2][(k+p)^2 - M_t^2] \,, \tag{14}$$

and $P_\pm = \frac{1}{2}(1 \pm \gamma_5)$. The coupling of the Z to the top quark is given in Eq. 5 and p is the external gauge boson momentum. Shifting momentum in the integral, $k' \to k - px$, and using Feynman parameters, the integral in $n = 4 - 2\epsilon$ dimensions becomes,

$$i\Pi_{ZZ}^{\mu\nu} = -N_c(\frac{-ig}{4c_W})^2(i)^2 \int \frac{d^n k'}{(2\pi)^n} \int_0^1 dx \\ \frac{[4k'^{\,2}(-1+\frac{\epsilon}{2})(R_t^2 + L_t^2) + 16 L_t R_t M_t^2]g^{\mu\nu} + ...}{(k'^{\,2} + p^2 x(1-x) - M_t^2)^2} \,, \tag{15}$$

where we retain only those terms contributing to $A_{ZZ}(0)$. The result proportional to M_t^2 is,

$$A_{ZZ}(p^2=0) = \frac{g^2 N_c}{32\pi^2 c_W^2}\left(\frac{4\pi}{M_t^2}\right)^{\epsilon}\frac{M_t^2}{\epsilon}(R_t - L_t)^2. \tag{16}$$

The analogous result for the W two-point function is,

$$A_{WW}(p^2=0) = \frac{g^2 N_c}{32\pi^2}\left(\frac{4\pi}{M_t^2}\right)^{\epsilon} M_t^2\left(\frac{1}{\epsilon}+\frac{1}{2}\right). \tag{17}$$

Combining Eqs. 16 and 17, the contribution to the ρ parameter which is proportional to M_t^2 is found from Eq. 11,[10]

$$\delta\rho = \frac{g^2 N_c}{64\pi^2}\frac{M_t^2}{M_W^2} = \frac{G_F N_c M_t^2}{8\sqrt{2}\pi^2}. \tag{18}$$

Experimentally[4] $\rho = 1.00126^{+.00234}_{-.0014}$ and so an upper limit on the top quark mass can be obtained from Eq. 18.

Many of the precision measurements shown in Fig. 3 are sensitive to M_t^2 and so a prediction for the top quark mass can be extracted quite precisely by combining many measurements. In fact, precision measurements were sensitive to the top quark mass *before* top was discovered at Fermilab! The agreement between the direct measurement of the top quark mass in the Fermilab collider experiments and the indirect prediction from the precision measurements (as shown in Fig. 4) is one of the triumphs of the Standard Model. It is interesting to note that a similar limit on the Higgs boson mass from precision measurements gives $M_h < 193\ GeV$ at the 95% confidence level.[3] Precision measurements depend logarithmically on the Higgs mass, and so it is much more difficult to bound the Higgs mass in this manner than it is to restrict the top quark mass. Increases in the experimental precisions of the top quark mass and the W boson mass in Run II measurements at the Tevatron will provide an improved bound on the Higgs boson mass, $\delta M_h/M_h \sim 40\%$.[11]

In the next sections, we discuss the discovery of the top quark at Fermilab and the experimental exploration of the top quark properties, both at Fermilab and the LHC and at a future high energy e^+e^- collider.

3. Top Quark Properties

3.1. *Hadronic Production*

The top quark was discovered in 1995 at Fermilab in $p\overline{p}$ collisions at $\sqrt{S} = 1.8\ TeV$.[1] This data set (called Run I) consists of an integrated luminosity of

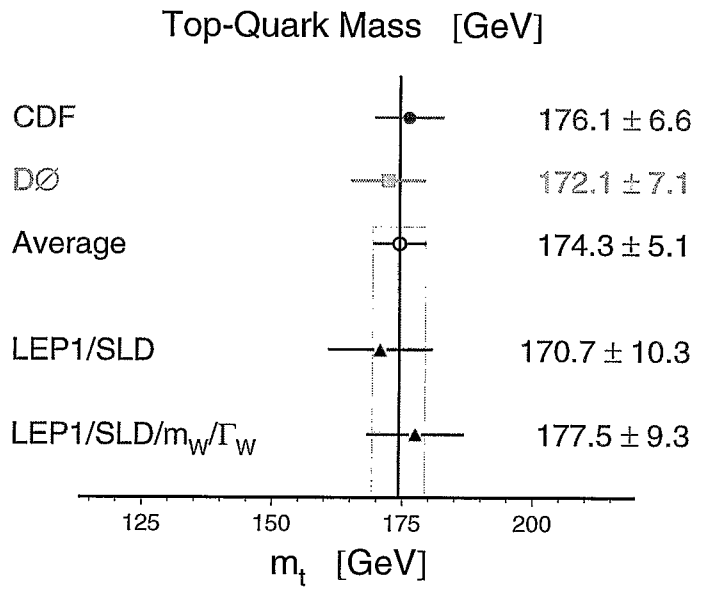

Figure 4. Measurements of the top quark mass at Fermilab (CDF and D0) and indirect predictions from precision measurements (LEP1, SLD and M_W).[3]

$L \sim 125\ pb^{-1}$. Both CDF and D0 are currently rediscovering the top quark in the Run II data set. Run II will produce roughly 500 clean top quark events for each inverse femtobarn of data and so precision measurements of many top quark properties will be possible.

In hadronic interactions, the top quark is produced by gluon fusion and by $q\bar{q}$ annihilation as shown in Fig. 5,

$$\begin{aligned} gg &\to t\bar{t} \\ q\bar{q} &\to t\bar{t}. \end{aligned} \tag{19}$$

The hadronic top quark production cross section, σ_H, at the Tevatron, $p\bar{p} \to t\bar{t}$, (or $pp \to t\bar{t}$ at the LHC) is found by convoluting the parton level cross section with the parton distribution functions (PDFs),

$$\sigma_H(S) = \Sigma_{ij} \int f_i(x_1,\mu) f_j(x_2,\mu) \hat{\sigma}_{ij}(x_1 x_2 S, \mu), \tag{20}$$

where the hadronic center of mass energy is S, the partonic center of mass energy is $s = x_1 x_2 S$, the parton distribution functions are $f_i(x,\mu)$, and the parton level cross section is $\hat{\sigma}_{ij}(s,\mu)$. The parameter μ is an unphysical

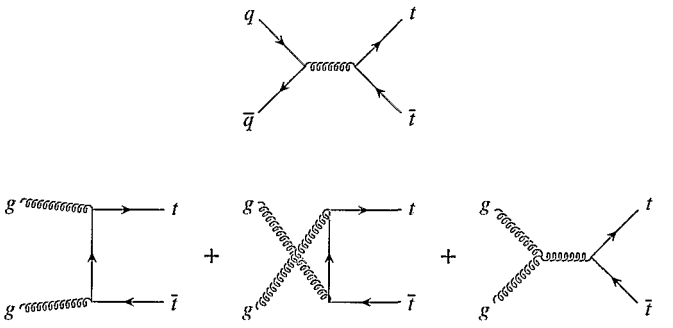

Figure 5. Feynman diagrams contributing to top quark pair production in hadron colliders.

renormalization/factorization scale. To $O(\alpha_s^2)$, the sum in Eq. 20 is over the $q\bar{q}$ and gg initial states shown in Fig. 5.

It is useful to parameterize the parton level cross section (to next-to-leading order in α_s) as,

$$\hat{\sigma}_{ij}(s,\mu) = \frac{\alpha_s^2(\mu)}{M_t^2}\left[h_{ij}^0(\rho) + h_{ij}^1\alpha_s(\mu) + h_{ij}^2\alpha_s(\mu)\log\left(\frac{\mu^2}{M_t^2}\right)\right] . \tag{21}$$

At lowest order, $O(\alpha_s^2)$, the parton level cross sections are,[12]

$$\begin{aligned} h_{q\bar{q}}^0 &= \frac{\pi\beta\rho}{27}(2+\rho) \\ h_{gg}^0 &= \frac{\pi\beta\rho}{192}\left[\frac{1}{\beta}(\rho^2+16\rho+16)\log\left(\frac{1+\beta}{1-\beta}\right) - 28 - 31\rho\right] \\ h_{qg}^0 &= 0 , \end{aligned} \tag{22}$$

where

$$\begin{aligned} \rho &= \frac{4M_t^2}{s} \\ \beta &= \sqrt{1-\rho} . \end{aligned} \tag{23}$$

The threshold condition is $\rho = 1$ and so $\hat{\sigma}_{ij}$ vanishes at threshold.

To any given order in $\alpha_s(\mu)$, the hadronic cross section σ_H must be independent of μ,

$$\frac{d\sigma_H}{d\log\mu^2} = 0. \tag{24}$$

Applying this restriction to Eq. 21 yields,

$$0 = \int \left\{ \frac{\partial f(x_1,\mu)}{\partial \log \mu^2} f(x_2,\mu) + f(x_1,\mu) \frac{\partial f(x_2,\mu)}{\partial \log \mu^2} \right\} \hat{\sigma}(x_1 x_2 S, \mu) dx_1 dx_2 + \int f(x_1,\mu) f(x_2,\mu) \frac{\partial \hat{\sigma}(x_1 x_2 S, \mu)}{\partial \log \mu^2} dx_1 dx_2 \ . \tag{25}$$

The scale dependence of the PDFs is governed by the Altarelli-Parisi evolution functions, $P_{ij}(z)$:

$$\frac{\partial f_i(x,\mu)}{\partial \log \mu^2} = \frac{\alpha_s}{2\pi} \Sigma_j \int_x^1 \frac{dy}{y} P_{ij}\left(\frac{x}{y}\right) f_j(y,\mu) \ . \tag{26}$$

Similarly, the scale dependence of the strong coupling constant, $\alpha_s(\mu)$, is governed by the evolution of the QCD β function.

$$\frac{\partial \alpha_s(\mu)}{\partial \log \mu^2} = -b_0 \alpha_s^2 \quad , \tag{27}$$

where $b_0 = \frac{(33-2n_{lf})}{12\pi}$, and n_{lf} is the number of light flavors. At next-to-leading order the scale dependence of the various terms must cancel, yielding a prediction for h_{ij}^2,

$$h_{ij}^2 = \frac{1}{2\pi} \left[4\pi b_0 h_{ij}^0(\rho) - \Sigma_k \int_\rho^1 dz h_{kj}^0\left(\frac{\rho}{z}\right) P_{ki}(z) - \Sigma_k \int_\rho^1 dz h_{ik}^0\left(\frac{\rho}{z}\right) P_{kj}(z) \right]. \tag{28}$$

Using the explicit forms of the Altarelli-Parisi evolution functions, combined with Eq. 22, we find[12]

$$\begin{aligned}
h_{q\bar{q}}^2 &= \frac{1}{2\pi} \left[\frac{16\pi\rho}{81} \log\left(\frac{1+\beta}{1-\beta}\right) + \frac{1}{9} h_{q\bar{q}}^0(\rho) \left(127 - 6n_{lf} + 48 \log\left(\frac{\rho}{4\beta^2}\right)\right) \right] \\
h_{gg}^2 &= \frac{1}{2\pi} \left[\frac{\pi}{192} \left\{ 2\rho\left(59\rho^2 + 198\rho - 288\right) \log\left(\frac{1+\beta}{1-\beta}\right) \right.\right. \\
&\quad + 12\rho\left(\rho^2 + 16\rho + 16\right) g_2(\beta) - 6\rho\left(\rho^2 - 16\rho + 32\right) g_1(\beta) \\
&\quad \left.\left. - \frac{4}{15}\beta\left(7449\rho^2 - 3328\rho + 724\right) \right\} - 12 h_{gg}^0(\rho) \log\left(\frac{\rho}{4\beta^2}\right) \right] \\
h_{qg}^2 &= \frac{1}{384} \left[\frac{4\rho}{9}\left(14\rho^2 + 27\rho - 136\right) \log\left(\frac{1+\beta}{1-\beta}\right) - \frac{32}{3}\rho(2-\rho) g_1(\beta) \right. \\
&\quad \left. - \frac{8\beta}{135}\left(1319\rho^2 - 3468\rho + 724\right) \right]
\end{aligned} \tag{29}$$

where we have defined,

$$g_1(\beta) = \log^2\left(\frac{1+\beta}{2}\right) - \log^2\left(\frac{1-\beta}{2}\right) + 2Li_2\left(\frac{1+\beta}{2}\right) - 2Li_2\left(\frac{1-\beta}{2}\right)$$
$$g_2(\beta) = Li_2\left(\frac{2\beta}{1+\beta}\right) - Li_2\left(\frac{-2\beta}{1-\beta}\right) . \quad (30)$$

The quantities h_{ij}^1 can only be obtained by performing a complete next-to-leading order calculation[12,13] and analytic results are not available, although a numerical parameterization is quite accurate. The strong coupling evaluated at the top quark mass is small, $\alpha_s(M_t) \sim 0.1$, and so a perturbative expansion converges rapidly. At energy scales significantly different from the top quark mass, there are also large logarithms of the form $(\alpha_s \log(\frac{M_t^2}{Q^2}))^n$, which can be summed to all orders to obtain an improved prediction for the cross section.[14] The inclusion of next-to-leading-logarithm effects reduces the scale dependence of the cross section to roughly $\pm 5\%$.[15]

Fig. 6 shows the Run I CDF and D0 measured top production cross sections and top quark mass compared with two theoretical predictions. The Run I $t\bar{t}$ cross sections are,[16]

$$\sigma_{t\bar{t}} = 6.5^{+1.7}_{-1.4}\ pb \qquad CDF$$
$$\sigma_{t\bar{t}} = 5.9 \pm 1.7\ pb \qquad D0\ . \quad (31)$$

The curves labelled NLO+NLL include some of the logarithms of the form $(\alpha_s \log(\frac{M_t^2}{Q^2}))^n$ and the agreement with the experimental results is clearly improved from the NLO prediction alone. An updated theoretical study including next-to-leading-logarithm resummation gives the prediction

$$\sigma_{t\bar{t}}(\sqrt{S} = 1.8\ TeV) = (4.81 - 5.29)\ pb \text{ for } M_t = 175\ GeV, \quad (32)$$

with the range in the prediction corresponding to $M_t/2 < \mu < 2M_t$.[15] The agreement between the predicted and the experimental production rates implies that the top quark is a color triplet, since that rate would be significantly different for a different color representation.

At the LHC, the subprocess $gg \to t\bar{t}$ dominates the production rate with 90% of the total rate and the cross section is large, $\sigma_{LHC} \sim 800\ pb$, yielding about 10^8 $t\bar{t}$ pairs/year. Because of the large rate, the LHC can search for new physics in top interactions. The large rate also has the implication that top production is often largest background to other new physics signals. A detailed understanding of the top quark signal is therefore a necessary ingredient of new physics searches.

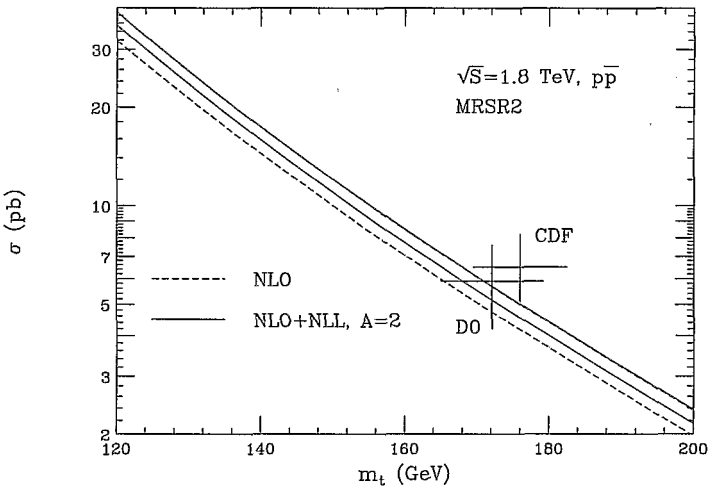

Figure 6. Fermilab Tevatron Run I cross sections for $p\bar{p} \to t\bar{t}$. The dashed line is the NLO prediction, while the solid lines incorporate the next-to-leading logarithms.[14]

3.2. *Weak Interactions of Top*

The weak interaction eigenstates are not mass eigenstates,

$$L = -\frac{g}{2\sqrt{2}}\Sigma_{q=d,s,b}\bar{t}\gamma^{\mu}(1-\gamma_5)V_{tq}qW_{\mu}^{+} + \text{h.c.} \tag{33}$$

and so the interaction of the top quark with a W boson and a light quark is proportional to the CKM mixing element, V_{tq}. Measurements of the decay rates of the top quark into the lighter quarks therefore translate directly into measurements of the CKM mixing angles.

The unitarity of the CKM matrix and the restriction to 3 generations of fermions gives a limit on V_{tb} from the measured values of $\mid V_{ub} \mid$ and $\mid V_{cb} \mid$:[4]

$$1 = \mid V_{ub} \mid^2 + \mid V_{cb} \mid^2 + \mid V_{tb} \mid^2 \tag{34}$$

giving,

$$0.9991 < \mid V_{tb} \mid < 0.9994\ . \tag{35}$$

If there are more than 3 generations, however, Eq. 34 is no longer valid and there is almost no limit from unitarity on V_{tb}.

Unitarity in the three generation model can be tested by measuring the ratio of the rate for top decays to the b quark to the rate for top decays to

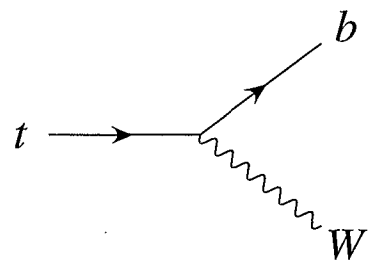

Figure 7. Feynman diagram for top decay to Wb.

lighter quarks,[17]

$$R_{tb} \equiv \frac{\Gamma(t \to Wb)}{\Gamma(t \to Wq)} = \frac{\mid V_{tb} \mid^2}{\mid V_{td} \mid^2 + \mid V_{ts} \mid^2 + \mid V_{tb} \mid^2}$$

$$= .94^{+.31}_{-.24} \quad (CDF) \tag{36}$$

This quantity can be measured at Fermilab by counting the number of tagged b's in a top quark event. Since the b quark lives approximately 1.5 ps, the b quark will travel 450 μm before decaying. The secondary b vertex can then be measured with a silicon vertex detector. Assuming unitarity of the CKM matrix, the denominator of Eq. 36 is 1, and the measurement can be interpreted as a measurement of V_{tb},

$$\mid V_{tb} \mid = .97^{+.15}_{-.12}, \tag{37}$$

consistent with Eq. 35.

If there is a fourth generation of quarks, (t', b'), the charge $-\frac{1}{3}$ b' is experimentally restricted to be heavier than $m_t - M_W$,[4] and so the top quark cannot decay into the b'. Then the denominator of R_{tb} need not equal 1, and the measurement implies only $\mid V_{tb} \mid >> \mid V_{ts} \mid$, $\mid V_{td} \mid$.

The direct measurement of V_{td} in single top production will be discussed in Section 3.6.

3.3. *Top Quark Decay*

The top quark is the only quark which decays before it can form a bound state. This is due to the very short lifetime of the top quark,

$$\tau_t \sim 5 \times 10^{-25} \; sec \; , \tag{38}$$

compared to the QCD time scale:

$$\tau_{QCD} \sim 3 \times 10^{-24}\ sec\ . \tag{39}$$

This is very different from the b quark system, where the b quark combines with the lighter quarks to form B mesons, which then decay.

Since $\mid V_{tb} \mid \sim 1$, the dominant decay of the top quark is

$$t(p) \rightarrow W^{\mu}(p_W) + b(p'), \tag{40}$$

The lowest order amplitude is shown in Fig. 7 and is,

$$A_0(t \rightarrow W^{\mu} b) = -\frac{g}{2\sqrt{2}} \overline{u}(p') \gamma^{\mu} (1 - \gamma_5) u(p)\ . \tag{41}$$

Squaring the amplitude, and summing over the W polarization vectors,

$$\Sigma \epsilon^{\mu}(p_W) \epsilon^{*\nu}(p_W) = -g^{\mu\nu} + \frac{p_W^{\mu} p_W^{\nu}}{M_W^2}, \tag{42}$$

gives the amplitude-squared,

$$\mid A_0(t \rightarrow Wb) \mid^2 = g^2 (M_t^2 - M_W^2) \left[1 + \frac{M_t^2}{2M_W^2} \right]\ . \tag{43}$$

The total decay width is

$$\Gamma_0(t \rightarrow Wb) = \left(\frac{1}{2} \right) \frac{1}{2M_t} \int \mid A_0(t \rightarrow Wb) \mid^2 (dPS_2)\ . \tag{44}$$

The factor of $\frac{1}{2}$ is the average over the initial top quark spin, and the phase space factor is,

$$(dPS_2) = \frac{M_t^2 - M_W^2}{8\pi M_t^2}\ . \tag{45}$$

Including the CKM mixing, the final result is then,

$$\Gamma_0(t \rightarrow bW^+) \sim \mid V_{tb} \mid^2 \frac{G_F M_t^3}{8\pi\sqrt{2}} \left(1 - \frac{M_W^2}{M_t^2} \right)^2 \left(1 + \frac{2M_W^2}{M_t^2} \right). \tag{46}$$

Higher order QCD corrections can be calculated in a straightforward manner and yield a precise prediction for the decay width,[9,18]

$$\Gamma(t \rightarrow bW^+) = \mid V_{tb} \mid^2 1.42\ GeV.$$

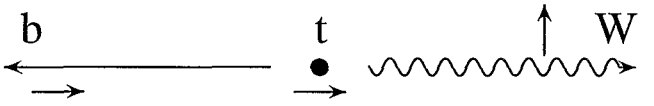

Figure 8. Spin vectors for longitudinally polarized W's produced in the decay $t \to Wb$.

3.4. *W Helicity in Top Quark Decay*

The helicity structure of the top quark decays is interesting because it yields information on the $V-A$ nature of the tbW vertex as is clear from Eq. 41. The top quark is produced through the weak interactions as a left-handed fermion (neglecting the b quark mass), which has spin opposite from the direction of the top quark motion.

If the W is produced as a longitudinal W (helicity 0), then its momentum and polarization vectors are (see Fig. 8):

$$\begin{aligned} p_W &= (E_W, 0, 0, \mid \vec{p}_W \mid) \\ \epsilon_L^W &= \frac{1}{M_W}(\mid \vec{p}_W \mid, 0, 0, E_W) \\ &\sim \frac{\mid \vec{p}_W \mid}{M_W} + O\left(\frac{M_W}{M_t}\right) . \end{aligned} \tag{47}$$

The amplitude for a top decaying into a longitudinal W is then,

$$\begin{aligned} A(t \to bW_L) &= -\frac{g}{2\sqrt{2}}\bar{b}\frac{p_W}{M_W}(1-\gamma_5)t + O\left(\frac{M_W}{M_t}\right) \\ &= -\frac{m_t}{\sqrt{2}v}\bar{b}(1+\gamma_5)t + O\left(\frac{M_W}{M_t}\right) . \end{aligned} \tag{48}$$

This gives the result that the decay of the top into longitudinal W's is,

$$\Gamma(t \to bW_L) \sim \frac{m_t^3}{v^2} . \tag{49}$$

The decay of the top quark into a positive helicity W, $h^W = +$, is forbidden by angular momentum conservation since a massless b quark is always left-handed, while the heavy top can be either left- or right-handed. This is illustrated in Fig. 9. CDF has measured the decay of the top quark to a right handed W and finds a result consistent with 0,[19]

$$BR(t \to bW_R) = .11 \pm 0.15 . \tag{50}$$

For a transversely polarized W, the polarization vector is given by,

$$\epsilon_\pm^W = \frac{1}{\sqrt{2}}(0, 1, \pm i, 0) . \tag{51}$$

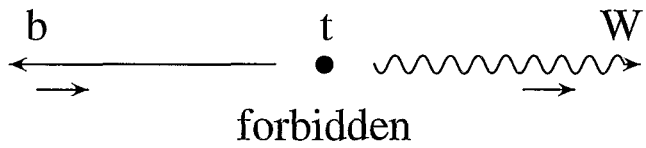

Figure 9. Spin vectors for positive helicity (right handed) W's produced in the decay $t \to Wb$. Conservation of angular momentum forbids this decay.

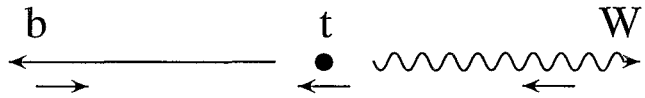

Figure 10. Spin vectors for transverse helicity W's produced in the decay $t \to Wb$.

This gives a decay rate,

$$\Gamma(t \to bW_T) \sim g^2 m_t \ . \tag{52}$$

Comparing Eqs. 49 and 52, it is clear that the rate for top decay to transverse W's is suppressed relative to that for decay to longitudinal W's,

$$\begin{aligned} F_0 &= \frac{\Gamma(t \to bW_L)}{\Gamma(t \to Wb)_{TOT}} \\ &= \frac{\frac{m_t^2}{2M_W^2}}{1 + \frac{m_t^2}{2M_W^2}} \\ &= 70.1\% \ . \end{aligned} \tag{53}$$

Can we measure this? The W helicity is correlated with the momentum of the decay leptons: $h^W = +$ gives harder charged leptons than $h^W = -$. A preliminary measurement of the polarization of the W's in top decay yields,[19]

$$F_0 = 91 \pm 37 \pm 13\% \ \ CDF, \tag{54}$$

consistent with Eq. 53. With 2 fb^{-1} of data from Run II at the Tevatron, a more definitive ($\sim 5\%$) measurement of F_0 will be possible.[20]

3.5. *Top Production and Decay*

The Tevatron and the LHC produce predominantly $t\bar{t}$ pairs, which decay almost entirely by $t \to Wb$ (since $\mid V_{tb} \mid \sim 1$),[a]

$$p\bar{p} \to t\bar{t} \to W^+W^-b\bar{b}. \tag{55}$$

It is useful to classify top quark events by the decay pattern of the W^+W^- pair:

- **Di-lepton**: Roughly 5% of the $t\bar{t}$ events fall into this category,

$$\begin{aligned} W^+ &\to l^+\nu, \quad l = e, \mu \\ W^- &\to l^-\nu \, . \end{aligned} \tag{56}$$

  Since $Br(W \to e\nu) + BR(W \to \mu\nu) \sim 22\%$, the 125 pb^{-1} at Run I of the Tevatron produced $\sim$ 625 $t\bar{t}$ events which yielded $\sim .22 \times .22 \times 625 \sim 30$ di-lepton events. These events are clean, but suffer from the small statistics.
- **lepton + jets**: This class of events comprises roughly 30% of the total,

$$W^{\pm} \to l^{\pm}\nu, \quad W^{\mp} \to jets \, . \tag{57}$$

  Lepton plus jet events are fully reconstructable and have small backgrounds. Assuming at least 1 b quark is tagged, CDF observed 34 such events in Run I, with an expected background of 8.[22] In Run II, with 2 fb^{-1}, there should be 1000 lepton+jets events/experiment. This increase from Run I results from higher luminosity, the higher cross section at $\sqrt{S} = 2 \; TeV$ compared to $\sqrt{S} = 1.8 \; TeV$, and upgraded detectors with improved capabilities for b-tagging.

  This channel produced the most precise measurement of the cross section for top pair production. The combined average from CDF and D0 at Run I is,

$$\sigma(p\bar{p} \to t\bar{t}) \mid_{\sqrt{S}=1.8 \; TeV} = 5.9 \pm 1.7 \; pb \tag{58}$$

- **All jets**: 44% of the events fall into this category. This class of events was observed by both CDF/D0 at Run I, with large backgrounds.

[a] Recent reviews of the experimental issues involved in top quark physics can be found in Ref. 21.

Table 2. Contributions to single top production at the Tevatron and the LHC.

	Tevatron, RunII	LHC
σ_{qb}	2.1 pb	238 pb
$\sigma_{q\overline{q}}$	.9 pb	10 pb
σ_{gb}	.1 pb	56 pb

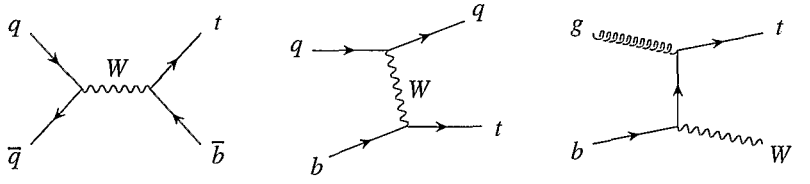

Figure 11. Feynman diagrams contributing to single top production at the Tevatron and the LHC.

3.6. *Single Top Production*

Single top production can provide a precise measurement of V_{tb}. The dominant production processes at the Tevatron are the t channel W exchange and the s channel $q\overline{q}$ annihilation shown in Fig. 11. At the LHC, the subprocess $gb \to tW$ is also important. The contributions (to NLO QCD) of the various subprocesses at the Tevatron and the LHC are given in Table 2.[23,24] All of these processes are proportional to $\mid V_{tb} \mid^2$.

Single top production was not observed in Run I, and both experiments set limits on the production rate. At Run II of the Tevatron, and at the LHC, single top production can be observed with a rate roughly half that of the $t\overline{t}$ rate and will lead to a measurement at the Tevatron of,

$$\mid \frac{\delta V_{tb}}{V_{tb}} \mid \sim 5\%$$

with 30 fb^{-1} of data. With 2 fb^{-1}, the Tevatron Run II should achieve an accuracy of $\mid \frac{\delta V_{tb}}{V_{tb}} \mid \sim 13\%$.[20]

3.7. *Measurements of M_t*

M_t is a fundamental parameter of the Standard Model, but the value is not predicted (except indirectly from precision measurements such as the ρ parameter discussed earlier). In the Standard Model, a precise value of M_t is important primarily for its role in precision electroweak observables and for the prediction for the Higgs boson mass extracted from these

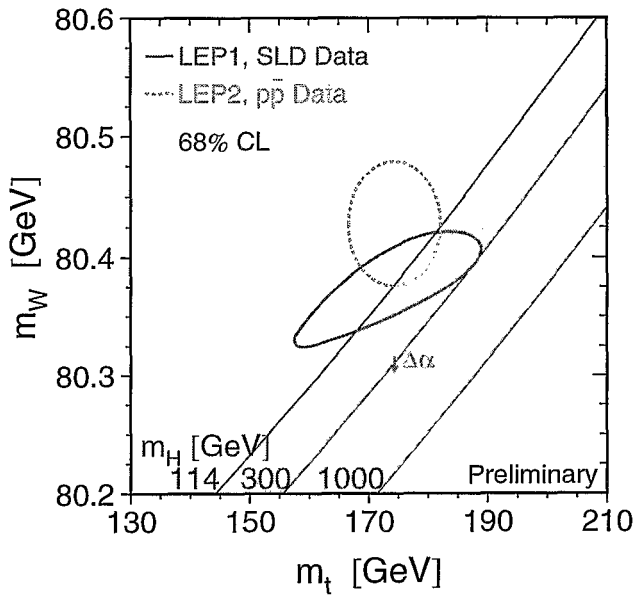

Figure 12. Implications of precision measurements of M_t and M_W on the indirect extraction of the Higgs boson mass. The Standard Model allows only the shaded region.[3]

measurements.[25] In extentions of the Standard Model, such as those discussed in Section 5, a precise knowledge of M_t plays a critical role in defining the parameters of the theory.

The top quark mass was measured in Run I at the Tevatron and the most accurate value of M_t comes from the single lepton+jets channel,[2]

$$\begin{aligned} M_t &= 176.1 \pm 4.8\ (stat) \pm 5.3\ (syst) \quad CDF \\ &= 173.3 \pm 5.6\ (stat) \pm 5.5\ (syst) \quad D0\ . \end{aligned} \tag{59}$$

In the lepton plus jets channel there is one unknown parameter (the longitudinal momentum of the ν coming from the W decay) and three constraints from the reconstruction of the W masses and the requirement that the reconstructed masses of the top and anti-top be identical, $M_t = M_{\bar{t}}$. The best value of the top quark mass found from combining all channels at the

Tevatron is,

$$M_t = 174.3 \pm 5.1\ GeV\ . \tag{60}$$

The systematic error is dominated by the uncertainty on the jet energy scale,

$$\begin{aligned} \pm 4.4\ GeV\ \ CDF \\ \pm 4\ GeV\ \ D0\ . \end{aligned} \tag{61}$$

With increased data from Run II, the mass measurement at the Tevatron will be improved to $\delta M_t \sim 3\ GeV$ with an integrated luminosity of 2 fb^{-1}.

Fig. 12 shows the impact of a precise measurement of the top quark mass combined with a W mass measurement for the prediction of the Higgs boson mass. Clearly, for the precision measurements of the W and top masses to be useful, the experimental error on both measurements needs to be comparable. The Higgs mass prediction extracted from precision measurements can be compared with the direct measurement of the Higgs mass at the LHC and the consistency of the Standard Model tested. Tevatron Run II with $2fb^{-1}$ should achieve accuracies:

$$\begin{aligned} \delta M_W &\sim 27\ MeV \\ \delta M_t &\sim 3\ GeV\ , \end{aligned} \tag{62}$$

yielding a prediction for the Higgs mass with an uncertainty of[25]

$$\frac{\delta M_h}{M_h} \sim 40\%\ . \tag{63}$$

The LHC will have large statistics on top quark production due to the large rate and can use the lepton+jets channel with 10 fb^{-1} of data to obtain a measurement[26]

$$\delta M_t \sim .07\ GeV\ . \tag{64}$$

3.8. *Top Spin Correlations*

When pair produced in either e^+e^- or $q\bar{q}$ collisions, the spins of the $t\bar{t}$ pair are almost 100% correlated.[27] The top decays before the spin can flip, and so spin correlations between the t and $\bar{t}$ result in angular correlations among the decay products. At threshold, the $t\bar{t}$ cross section is s-wave, and the e^+e^- or $q\bar{q}$ spins are translated directly to the $t\bar{t}$ spins. The incoming $q, \bar{q}$ have opposite helicities, since they are interacting through a gauge interaction and the $t\bar{t}$ spins aligned along the beamline. At high energy,

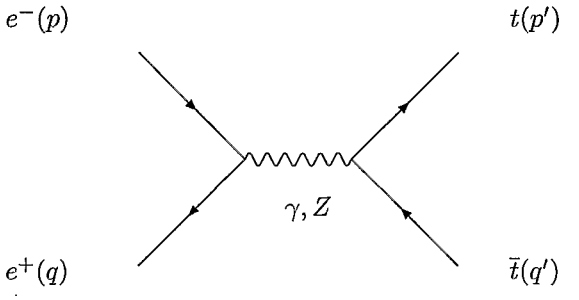

Figure 13. Lowest order Feynman diagram for $e^+e^- \to t\bar{t}$.

$\sqrt{s} >> m_t$, the top mass is irrelevant and the $t, \bar{t}$ must have opposite helicities. Finding the correct basis for intermediate energies is subtle, however.

4. The Top Quark as a QCD Laboratory

The production and decay mechanisms for the top quark in both e^+e^- and hadronic collisions are well understood and so the top quark system provides an ideal laboratory for studying perturbative QCD. This section contains a pedagogical treatment of the $O(\alpha_s)$ next- to- leading order (NLO) QCD corrections to the process $e^+e^- \to t\bar{t}$.[28] This process is particularly simple since the QCD corrections affect only the final state. The calculation is performed using the two cut-off phase space slicing (PSS) algorithm for evaluating the real gluon emission diagrams.[29,30] The total rate for $e^+e^- \to t\bar{t}$ tests our understanding of perturbative QCD and additionally the threshold behavior of the total cross section can be used to obtain a precise measurement of M_t, along with information on $\alpha_s(M_t)$ and the $t\bar{t}h$ Yukawa coupling. An understanding of the QCD corrections are crucial for these interpretations.

As a second example of the role of QCD in top quark physics, we consider the associated production of a $t\bar{t}$ pair along with a Higgs boson, h. The $t\bar{t}h$ Yukawa coupling is a fundamental parameter of the theory and probes the mechanism of mass generation, since in the Standard Model, $g_{tth} = \frac{M_t}{v}$. The processes $e^+e^- \to t\bar{t}h$ and $pp(p\bar{p}) \to t\bar{t}h$ provide sensitive measurements of the top quark- Higgs coupling and can be used to verify the correctness of the Standard Model and to search for new physics in the top quark and Higgs sectors. The importance of the QCD NLO corrections to $t\bar{t}h$ production is discussed at the end of this section.

4.1. *NLO QCD corrections to* $e^+e^- \to t\bar{t}$

The Born amplitude for $e^+e^- \to t\bar{t}$ proceeds via $s-$ channel γ and Z exchange, as shown in Fig. 13. The dominant contribution at $\sqrt{s} = 500\ GeV$ is from γ exchange and so for simplicity we will neglect the Z contribution here. (The complete $O(\alpha_s)$ result, including the contribution from $Z-$ exchange can be found in Refs. 28 and 30.) The electron mass can also be neglected. The lowest order amplitude is:

$$A_{LO}(e^+e^- \to t\bar{t}) = \frac{e^2 Q_e Q_t}{s} \overline{v}(q)\gamma^\mu u(p)\overline{u}(p')\gamma_\mu v(q')\delta_{ij} \ ,$$

where i, j are the color indices of the outgoing top quarks. It is simplest to work in the center-of-mass frame of the incoming e^+e^- pair, where the 4−momenta of the particles are given by:

$$\begin{aligned} p &= \frac{\sqrt{s}}{2}(1,0,0,1) \\ q &= \frac{\sqrt{s}}{2}(1,0,0,-1) \\ p' &= \frac{\sqrt{s}}{2}(1,0,\beta\sin\theta,\beta\cos\theta) \\ q' &= \frac{\sqrt{s}}{2}(1,0,-\beta\sin\theta,-\beta\cos\theta) \end{aligned}$$

with

$$\begin{aligned} s &= (p+q)^2 \\ \beta &= \sqrt{1-\frac{4M_t^2}{s}} \end{aligned} \tag{65}$$

and θ is the angle of the top quark emission with respect to the electron beam direction. The threshold condition is defined by $\beta = 0$.

It is straightforward to find the tree level amplitude-squared in $n = 4-2\epsilon$ dimensions, (summed over colors),

$$\mid A_{LO} \mid^2 = 64\pi^2\alpha^2 Q_t^2 N_c \Big[2(1-\epsilon) + \beta^2(\cos^2\theta - 1)\Big] \ . \tag{66}$$

The color factor is $N_c = 3$. The corresponding total cross section is:

$$\sigma_{LO} = \frac{1}{2s}\int \mid A_{LO} \mid^2 (dPS)_2. \tag{67}$$

Integrating over the two body phase space,

$$(dPS)_2 = \frac{2^{2\epsilon}}{16\pi}\left(\frac{4\pi}{s}\right)^\epsilon \beta^{1-2\epsilon}\frac{1}{\Gamma(1-\epsilon)}\int_0^\pi \sin^{1-2\epsilon}\theta d\theta, \tag{68}$$

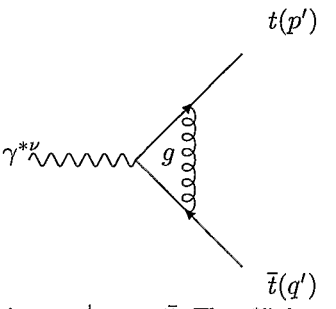

Figure 14. Vertex correction to $e^+e^- \to t\bar{t}$. The $\gamma^{*\nu}$ denotes an off-shell photon which is connected to the initial e^+e^- state.

and including a factor of $\frac{1}{4}$ for the average over the initial electron spins, gives a total rate,

$$\sigma_{LO}(e^+e^- \to t\bar{t}) = \frac{\beta}{32\pi s}\frac{1}{4}\int_{-1}^{1} d\cos\theta \mid A_{LO} \mid^2 + O(\epsilon)$$

$$= \frac{2\pi N_c \alpha^2 Q_t^2}{3s}\beta(3-\beta^2) + O(\epsilon).$$

The $O(\epsilon)$ terms which we have neglected will be important in computing the $O(\alpha_s)$ QCD corrections. The cross section vanishes at threshold, $\beta \to 0$, and decreases with increasing energy, $\sigma \sim \frac{1}{s}$. This has the obvious implication that the higher energy an e^+e^- collider, the larger the required luminosity.

4.2. $O(\alpha_s)$ corrections to $e^+e^- \to t\bar{t}$

The $O(\alpha_s)$ corrections to $e^+e^- \to t\bar{t}$ contain both real and virtual contributions:

$$\sigma_{NLO} = \sigma_{LO} + \sigma_{virtual} + \sigma_{real}. \tag{69}$$

The one-loop virtual contribution consists of a vertex correction and a wave-function renormalization of the top quark leg. The vertex correction is shown in Fig. 14 and can be parameterized as:

$$A_{vertex} = eQ_e\overline{v}(q)\gamma_\nu u(p)\frac{1}{s}\Gamma^\nu(p',q') \tag{70}$$

with,

$$\Gamma_\nu(p',q') = (-eQ_t)\delta_{ij}g_s^2 C_F[N]\overline{u}(p')\left[A\frac{(p'+q')_\nu}{2M_t} + B\gamma_\nu\right]v(q') \tag{71}$$

where the normalization is,

$$[N] \equiv \frac{1}{16\pi^2}\left(\frac{4\pi\mu^2}{M_t^2}\right)^{\epsilon}\Gamma(1+\epsilon) \tag{72}$$

and

$$C_F = \frac{N_c^2-1}{2N_c} = \frac{4}{3}\ . \tag{73}$$

is the color factor for the vertex diagram. The parameter μ is an arbitrary renormalization scale. Explicit calculation gives the results,[28,30]

$$\begin{aligned}
A &= (\beta - \frac{1}{\beta})\Lambda_\beta \\
\Lambda_\beta &\equiv \log\left(\frac{1-\beta}{1+\beta}\right) \\
B &= \frac{1}{\epsilon}\left[1-(\frac{1}{\beta}+\beta)\Lambda_\beta\right] - 3\beta\Lambda_\beta + \left(\frac{1}{\beta}+\beta\right)\left[-\frac{1}{2}\Lambda_\beta^2 + 2\Lambda_\beta\log\left(\frac{2\beta}{1+\beta}\right)\right. \\
&\quad \left. +2Li_2(\frac{1-\beta}{1+\beta}) + \frac{2\pi^2}{3}\right] \\
&\equiv \frac{B_\epsilon}{\epsilon} + B_{fin}\ .
\end{aligned}$$

The di-logarithm is defined by,

$$Li_2(x) = -\int_0^1 dz \frac{1}{1-xz}\ . \tag{74}$$

The $O(\alpha_s)$ contribution to the virtual cross section is the interference of the vertex correction with the lowest order result. (The A term of Eq. 71 does not contribute to the interference with the lowest order result when the electron mass is neglected).

$$\begin{aligned}
\sigma_{vertex} &= 2\left(\frac{1}{2s}\right)\left(\frac{1}{4}\right)\int (dPS)_2 A_{LO} A^*_{vertex} \\
&= \frac{\alpha_s}{2\pi}\left(\frac{4\pi\mu^2}{M_t^2}\right)^{\epsilon} C_F\Gamma(1+\epsilon)\sigma_{LO}\left[\frac{B_\epsilon}{\epsilon} + B_{fin}\right]\ .
\end{aligned} \tag{75}$$

Note that the $O(\epsilon)$ terms from the lowest order amplitude and from the 2-particle phase space combine with the $\frac{B_\epsilon}{\epsilon}$ term to give a finite contribution to σ_{vertex}.

The wavefunction renormalization for the top quark must also be included in the virtual correction, as shown in Fig.

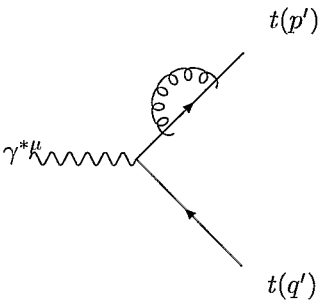

Figure 15. Feynman diagram for top quark wavefunction renormalization.

15. This diagram gives a multiplicative correction to the lowest order rate. Using the on-shell renormalization scheme,

$$\sigma_Z = 2\delta Z_{tt}\sigma_{LO}, \tag{76}$$

where

$$\begin{aligned}\delta Z_{tt} &= \frac{\partial \Pi(p^2)}{\partial p^2} \mid p^2 = M_t^2 \\ &= -\frac{\alpha_s}{4\pi}\left(\frac{4\pi\mu^2}{M_t^2}\right)^{\epsilon} C_F \Gamma(1+\epsilon)\left(\frac{3}{\epsilon}+4\right) . \end{aligned} \tag{77}$$

The total virtual contribution is thus:[28,30]

$$\begin{aligned}\sigma_{VIRT} &= \sigma_{vertex} + \sigma_Z \\ &= \sigma_{LO}\frac{\alpha_s}{2\pi}\Gamma(1+\epsilon)C_F\left(\frac{4\pi\mu^2}{M_t^2}\right)^{\epsilon}\left[(-3+B_\epsilon)\frac{1}{\epsilon}-4+B_{fin}\right] . \end{aligned} \tag{78}$$

4.3. *Real contributions*

The virtual singularities of Eq. 78 are cancelled by those arising from real gluon emission, $e^+e^- \to t\bar{t}g$. A sample diagram of this type is shown in Fig. 16. The real gluon emission diagram of Fig. 16 contains a fermion propagator on the outgoing top quark leg of the form:

$$\frac{1}{(p'+p_g)^2 - M_t^2} = \frac{1}{2p'\cdot p_g} = \frac{1}{2E'E_g(1-\hat{\beta}\cos\hat{\theta})},$$

where E' and E_g are the energies of the outgoing top quark and gluon, $\hat{\theta}$ is the angle between them, and $\hat{\beta} = \sqrt{1-\frac{M_t^2}{E'^2}}$. Because of the massive top quark, $\hat{\beta} \neq 1$, and this diagram has no collinear singularity as $\hat{\theta} \to 0$. There is, however, a soft singularity as the energy of the gluon vanishes, $E_g \to 0$.

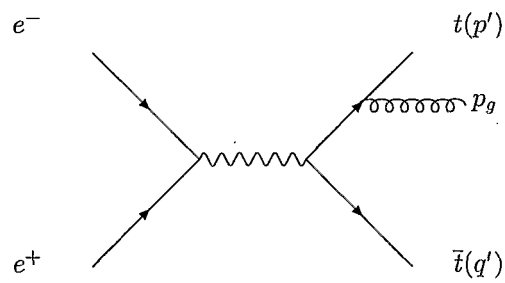

Figure 16. Sample Feynman diagram for real gluon emission in the process $e^+e^- \to t\bar{t}g$.

The soft singularity is regulated using a technique called phase space slicing (PSS).[30] This method divides the gluon phase space into a soft gluon plus a hard gluon region:

$$\sigma_{real} \equiv \sigma_{soft} + \sigma_{hard} \ . \tag{79}$$

The soft region is defined by the energy of the emitted gluon,

$$E_g < \delta_s \frac{\sqrt{s}}{2}, \tag{80}$$

while the hard region is the remainder of the gluon phase space.

$$E_g > \delta_s \frac{\sqrt{s}}{2} \ . \tag{81}$$

The separation into hard and soft regions depends on the arbitrary parameter δ_s. Individually, σ_{soft} and σ_{hard} depend on the cutoff, δ_s, and the independence of the sum is a check on the calculation. δ_s must be small enough that terms of $O(\delta_s)$ can be neglected, while large enough to prevent numerical instabilities. σ_{hard} is finite and can be evaluated numerically using standard Monte Carlo techniques.

In the soft gluon regime, the cross section can be evaluated analytically. The three body phase space is evaluated in the soft limit in the rest frame of the incoming e^+e^-:

$$p + q = p' + q' + p_g, \tag{82}$$

giving a gluon energy of

$$\begin{aligned} E_g &= \left(\frac{s - s_{p'q'}}{2\sqrt{s}} \right) \\ s_{p'q'} &= (p' + q')^2 \ . \end{aligned} \tag{83}$$

The 3-body phase space in the soft limit can be separated into a 2 body phase space factor times a soft phase space factor:[31]

$$(dPS)_3 = \int \frac{d^{n-1}p'}{2E_{p'}(2\pi)^{n-1}} \int \frac{d^{n-1}q'}{2E_{q'}(2\pi)^{n-1}} \cdot (2\pi)^n \delta^n(p+q-p'-q'-p_g) \cdot \int \frac{d^{n-1}p_g}{2E_g(2\pi)^{n-1}} \ . \tag{84}$$

For the soft limit, we set the gluon momenta $p_g = 0$ in the delta function and the phase space then factorizes:

$$(dPS)_3(soft) = (dPS)_2 \int \frac{d^{n-1}p_g}{2E_g(2\pi)^{n-1}} \ . \tag{85}$$

The phase space is most easily evaluated by choosing an explicit representation for the gluon momentum,

$$p_g = E_g(1, ..., \sin\theta_1 \sin\theta_2, \sin\theta_1 \cos\theta_2, \cos\theta_1). \tag{86}$$

yielding,[32]

$$\begin{aligned} d^{n-1}p_g &= d \mid \vec{p}_g \mid\mid \vec{p}_g \mid^{n-2} d\Omega_{n-2} \\ &= dE_g E_g^{n-2} \sin^{n-3}\theta_1 d\theta_1 \sin^{n-4}\theta_2 d\theta_2 d\Omega_{n-4} \end{aligned} \tag{87}$$

where,

$$\Omega_{n-4} = \frac{2\pi^{(n-3)/2}}{\Gamma(\frac{n-3}{2})}. \tag{88}$$

The integrals can be performed analytically to find the three body phase space in soft limit:[32]

$$(dPS)_3(soft) = (dPS)_2 \left(\frac{4\pi}{s}\right)^{\epsilon} \left(\frac{1}{8\pi^2}\right) \frac{\Gamma(1-\epsilon)}{\Gamma(1-2\epsilon)} dPS_{soft}$$

$$dPS_{soft} = \frac{1}{\pi}\left(\frac{s}{4}\right)^{\epsilon} \int_0^{\delta_s \frac{\sqrt{s}}{2}} dE_g E_g^{1-2\epsilon} \cdot \sin^{1-2\epsilon}\theta_1 d\theta_1 \sin^{-2\epsilon}\theta_2 d\theta_2 \ . \tag{89}$$

Note that the soft phase space depends explicitely on the cut-off δ_s through the limit on the E_g integral.

The soft phase space must be combined with the amplitude for $e^+e^- \to t\bar{t}g$ in $p_g \to 0$ limit:

$$A_{soft} = \frac{e^2 Q_e Q_t}{s} g_s T^A \overline{v}(q)\gamma_\mu u(p) \cdot \overline{u}(p')\left\{\gamma^\sigma \frac{(p' + p_g + M_t)}{(p' + p_g)^2 - M_t^2}\gamma^\mu + \gamma^\mu \frac{(-q' - p_g + M_t)}{(q' + p_g)^2 - M_t^2}\gamma^\sigma\right\} v(q') \to g_s T^A \left[\frac{p'^\sigma}{p' \cdot p_g} - \frac{q'^\sigma}{q' \cdot p_g}\right] A_{LO} \tag{90}$$

where we have set $p_g = 0$ in the numerator. The approximation of retaining only the most singular contributions is known as the eikonal (or double pole) approximation.[33] The soft limit of the amplitude always factorizes in this manner into a factor multiplying the lowest order amplitude.

The soft amplitude-squared is

$$\mid A_{soft} \mid^2 = g_s^2 Tr(T^A T^A) \mid A_{LO} \mid^2 \cdot \left[-\frac{M_t^2}{(p' \cdot p_g)^2} - \frac{M_t^2}{(q' \cdot p_g)^2} + \frac{s - 2M_t^2}{p' \cdot p_g q' \cdot p_g}\right] \tag{91}$$

giving the cross section in the soft limit,[b]

$$\sigma_{soft} = \frac{1}{2s}\left(\frac{1}{4}\right) \int \mid A_{soft} \mid^2 (dPS)_3(soft) \ . \tag{92}$$

The problem reduces to evaluating the soft integrals. A typical integral is

$$I^{soft} \equiv \int \frac{1}{(p' \cdot p_g)^2} dPS_3(soft) \ . \tag{93}$$

Since the phase space and the amplitude squared are Lorentz invariant, we are free to chose any convenient frame. We use

$$p_g = E_g(1, ... \sin\theta_1 \sin\theta_2, \sin\theta_1 \cos\theta_2, \cos\theta_1)$$
$$p' = \frac{\sqrt{s}}{2}(1, 0, 0, \beta) \tag{94}$$

[b] As always, the factor of 1/4 is the spin average.

and the soft integral is,

$$
\begin{aligned}
I^{soft} &= \int \frac{1}{(p' \cdot p_g)^2} dPS_3(soft) \\
&= \frac{1}{\pi}\left(\frac{s}{4}\right)^{\epsilon} \int_0^{\delta_s \frac{\sqrt{s}}{2}} dE_g E_g^{1-2\epsilon} \sin^{1-2\epsilon}\theta_1 d\theta_1 \sin^{-2\epsilon} d\theta_2 \\
&\quad \cdot \left(\frac{4}{sE_g^2}\right) \frac{1}{(1-\beta\cos\theta_1)^2} \\
&= \frac{2}{M_t^2}\left(-\frac{1}{2\epsilon} + \log(\delta_s) + \frac{1}{2\beta}\Lambda_\beta\right) + O(\delta_s, \epsilon) \ . \qquad (95)
\end{aligned}
$$

The complete set of soft integrals relevant for this process is given in the appendix of Ref. 34.

The soft cross section is

$$
\sigma_{soft} = \sigma_{LO}\frac{\alpha_s}{2\pi} C_F \left(\frac{4\pi\mu^2}{s}\right)^{\epsilon} \frac{\Gamma(1-\epsilon)}{\Gamma(1-2\epsilon)}\left[\frac{C_\epsilon}{\epsilon} + C_{fin}\right], \qquad (96)
$$

where $B_\epsilon = -C_\epsilon$ so the sum of virtual plus soft contributions is finite. The finite contribution, C_{fin}, depends on δ_s and is given by[30]

$$
\begin{aligned}
C_{fin} &= -4\log(\delta_s) - \frac{2}{\beta}\Lambda_\beta - 2\left(\frac{1}{\beta} + \beta\right) \\
&\quad \cdot \left[Li_2\left(\frac{2\beta}{1+\beta}\right) + \frac{\Lambda_\beta^2}{4} + \log(\delta_s)\Lambda_\beta\right] + O(\delta_s) \ . \qquad (97)
\end{aligned}
$$

The complete $O(\alpha_s)$ result for $e^+e^- \to t\bar{t}$ is then,

$$
\sigma_{NLO} = \sigma_{LO} + \sigma_{virtual} + \sigma_{soft} + \sigma_{hard} \ . \qquad (98)
$$

The combination $\sigma_{soft} + \sigma_{hard}$ is independent of δ_s, while the $\frac{1}{\epsilon}$ poles cancel between $\sigma_{soft} + \sigma_{virtual}$.

This example, $e^+e^- \to t\bar{t}$, is simple enough that it could have been done analytically without the approximation of phase space slicing[28]. Phase space slicing, however, is useful for more complicated examples and also to construct Monte Carlo distributions beyond the leading order.

4.4. *Threshold Scan in $e^+e^- \to t\bar{t}$*

The energy dependence of the cross section for $e^+e^- \to t\bar{t}$ at threshold depends sensitively on the parameters of the top sector. The location of the peak depends on M_t, while the height of the peak depends on Γ_t. The problem is that the location of the peak as a function of center-of-mass

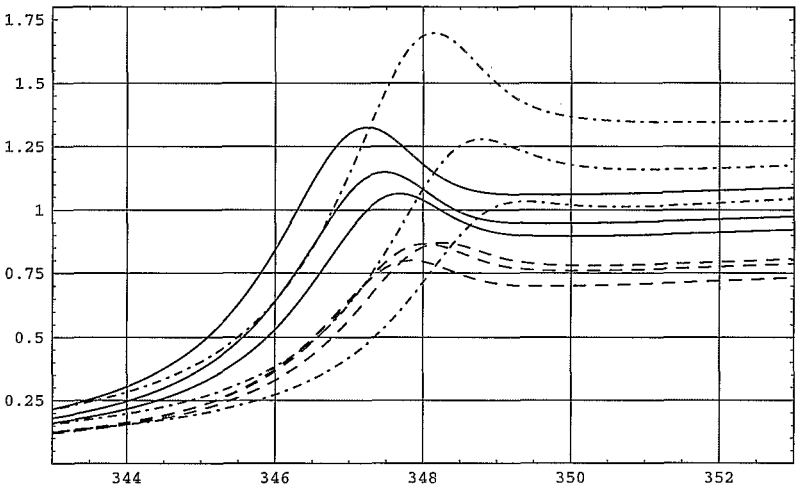

Figure 17. Cross section for $e^+e^- \to t\bar{t}$ as a function of the center-of-mass energy in GeV using the pole mass definition for the top quark mass at lowest order (dot-dashed), NLO (dashed), and NNLO (solid). The vertical axis shows $\sigma(e^+e^- \to t\bar{t})/\sigma_{pt}$, where $\sigma_{pt} = 4\pi\alpha^2/3s$. The three sets of curves at each order represent the variation with the renormalization scale μ, ($\mu = 15,\ 30$, and 60 GeV).[37]

energy shifts at higher orders and there is a large renormalization scale dependence to the prediction as seen in Fig. 17.[35]

At threshold, $\beta \to 0$, the theory possesses two small parameters: α_s and β and the cross section diverges at $O(\alpha_s)$,[9]

$$\sigma(e^+e^- \to t\bar{t})\mid_{\beta\to 0} = \sigma_{LO}\left(1 + \frac{2\pi\alpha_s}{3\beta}\right). \tag{99}$$

This divergence as $\beta \to 0$ is known as a Coulomb singularity and non-relativistic quantum mechanics can be used to sum the leading contributions in powers of $\frac{1}{\beta}$.[36]

Beyond lowest order in α_s, the predictions are quite sensitive to the precise definition of the top quark mass. The most straightforward definition is the pole mass appearing in the top quark propagator,

$$D(p) = \frac{i}{p - M_t\mid_{pole} - \Sigma(p)}\ . \tag{100}$$

The pole mass, $M_t\mid_{pole}$, is measured by reconstructing the four-momenta of top quark decay products. This definition of the top quark mass is, however, uncertain by QCD hadronization effects, $O(\Lambda_{QCD})$. These effects connect the top quark with its decay products. Even more disturbing is

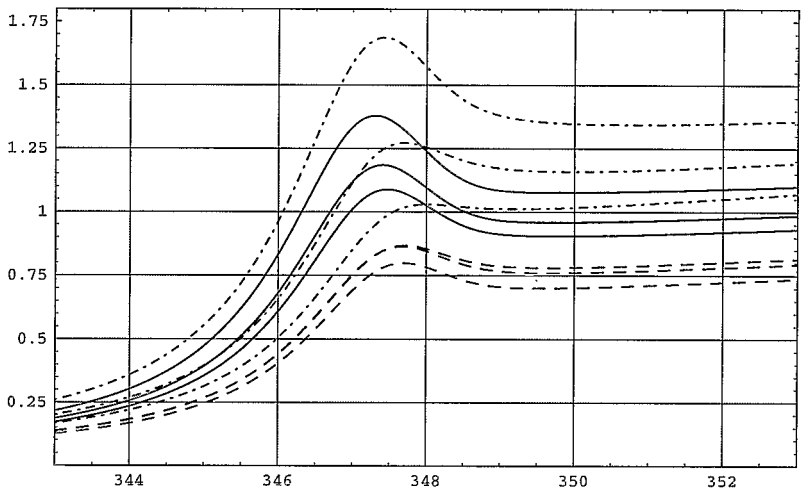

Figure 18. Cross section for $e^+e^- \to t\bar{t}$ as a function of the center-of-mass energy in GeV using the 1S mass definition for the top quark mass at lowest order (dot-dashed), NLO (dashed), and NNLO (solid). The vertical axis shows $\sigma(e^+e^- \to t\bar{t})/\sigma_{pt}$, where $\sigma_{pt} = 4\pi\alpha^2/3s$. The three sets of curves at each order represent the variation with the renormalization scale μ, ($\mu = 15,\ 30$, and 60 GeV). [37]

the fact that the location and height of the peak in the $e^+e^- \to t\bar{t}$ cross section change significantly between lowest order, NLO, and NNLO as seen in Fig. 17. A better definition of the top quark mass is the short distance $1S$ mass:[37,38]

$$m_{1S} = M_t\,|_{pole}\,(1 - \frac{2\alpha_s^2}{9}....)\ . \tag{101}$$

Using this mass definition, the cross section for $e^+e^- \to t\bar{t}$ peaks at $2m_{1S}$ and the location of the peak does not shift at NLO or NNLO, as seen in Fig. 18.

The NNLO result still has roughly a 20% scale uncertainty. It is estimated that by scanning the threshold dependence of the cross section for $e^+e^- \to t\bar{t}$ a measurement with the accuracy $\delta M_t \sim 200\ MeV$ can be made with an integrated luminosity of $L = 50\ fb^{-1}$. This is to be compared with the expected accuracy of the LHC measurement, $\delta M_t \sim 1 - 2\ GeV$.[26] A precise measurement of the top quark mass is of interest primarily because of its implications for electroweak precision measurements.[25]

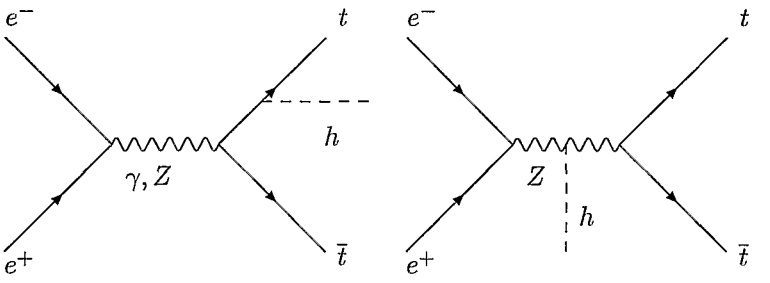

Figure 19. Contributions to $e^+e^- \to t\bar{t}h$ at lowest order.

4.5. *tth production in e^+e^- and pp collisions*

In many models with physics beyond the Standard Model, the Higgs coupling to the top quark is significantly different from that in the Standard Model. In the Standard Model, the fermion-Higgs Yukawa couplings are,

$$L = -g_{ffh}\overline{\psi}\psi h \tag{102}$$

where

$$g_{ffh} = \frac{M_f}{v} \,. \tag{103}$$

Since the top quark is the heaviest quark, it has the largest Yukawa coupling to the Higgs boson. It is important to measure this coupling accurately in order to verify that the Higgs mechanism is the source of fermion masses.

The Higgs boson couplings to the lighter quarks can be tested by measuring the Higgs decays to fermion pairs. This is not possible, however, for the top-fermion coupling. Only for very heavy Higgs bosons ($M_h > 2M_t$) is the decay $h \to t\bar{t}$ kinematically accessible, and the branching ratio of the Higgs into $t\bar{t}$ pairs is significantly smaller than that into gauge boson pairs. It does not appear feasible to measure g_{tth} through this channel. The most promising prospect for measuring the top quark Yukawa coupling is $t\bar{t}h$ production in e^+e^- and pp (or $p\bar{p}$) collisions.

4.6. *$t\bar{t}h$ at an e^+e^- collider*

At an e^+e^- collider, $t\bar{t}h$ associated production occurs through s-channel γ and Z exchange, as shown in Fig. 19. The contribution from Z exchange is a few percent of the total rate and will be neglected here. With this assumption, the rate is directly proportional to g^2_{tth}. In order to interpret the cross section as a measurement of g_{tth}, however, it is necessary to include

the QCD corrections which are potentially of the same order of magnitude as new physics effects which may change g_{tth} from the SM prediction. The NLO QCD result includes virtual and real gluon corrections on the outgoing $t, \bar{t}$ legs. The calculation follows that of the previous section for $e^+e^- \to t\bar{t}$, although in this case the virtual calculation also includes box diagrams. These corrections have been found in Refs. 39 and 40 and can be parameterized as

$$K \equiv \frac{\sigma_{NLO}}{\sigma_{LO}} = 1 + \alpha_s(\mu) F(s, M_t^2, M_h^2) \ . \tag{104}$$

The parameter μ is an unphysical renormalization scale and, at this order, the only dependence on μ is in the running of $\alpha_s(\mu)$. For $M_h = 120\ GeV$, and μ ranging from M_t to $\sqrt{s}$,

$$\begin{aligned} K(\sqrt{s} = 500\ GeV) &\sim 1.4 - 1.5 \\ K(\sqrt{s} = 1\ TeV) &\sim .8 - .9 \ . \end{aligned} \tag{105}$$

The NLO results for $t\bar{t}h$ production in e^+e^- collisions are shown in Fig. 20. The rate is quite small and has a maximum value for $\sqrt{s} \sim 700 - 800\ GeV$ for M_h in the $120\ GeV$ region.

In order to measure the top quark Yukawa coupling in e^+e^- collisions, we consider the final state

$$e^+e^- \to t\bar{t}h \to W^+W^-b\bar{b}b\bar{b} \ . \tag{106}$$

The events are then classified according to the W decays, in an analogous manner to that discussed in Section 3.5 for top quark decays. Since the event rate is quite small, it is advantageous to combine hadronic and semi-leptonic W decay channels.[41,42] At $\sqrt{s} = 800\ GeV$, an integrated luminosity of $L = 1000\ fb^{-1}$, can measure the coupling to an accuracy of[41]

$$\frac{\delta g_{tth}}{g_{tth}} \sim 5.5\% \ . \tag{107}$$

At a lower energy, $\sqrt{s} = 500\ GeV$, the rate is considerably smaller and even with an integrated luminosity of $L = 1000\ fb^{-1}$, the precision is quite poor,[42]

$$\frac{\delta g_{tth}}{g_{tth}} \sim 20\% \ , \tag{108}$$

for $M_h = 120\ GeV$.

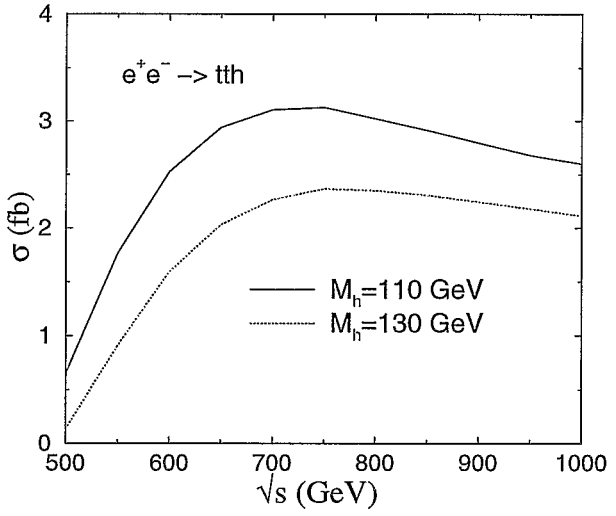

Figure 20. NLO rate for $e^+e^- \to t\bar{t}h$ as a function of center of mass energy.[39]

4.7. $pp \to t\bar{t}h$ at NLO

The QCD corrections to $pp \to t\bar{t}h$ (or $p\bar{p} \to t\bar{t}h$) can be calculated in a similar fashion to those for $e^+e^- \to t\bar{t}h$. In the hadronic case, however, the calculation is complicated by the existence of strong interactions in the initial state. In this section, we discuss the treatment of initial state singularities in hadron collisions. The ingredients of an NLO calculation for pp or $p\bar{p} \to t\bar{t}h$ are:[34,43]

- $\sigma_{virtual}$: This contains all of the one-loop diagrams contributing to the process. Finite diagrams, or diagrams which contain only ultraviolet singularities, can be evaluated numerically.[44] Diagrams which contain infrared singularities must be evaluated analytically.

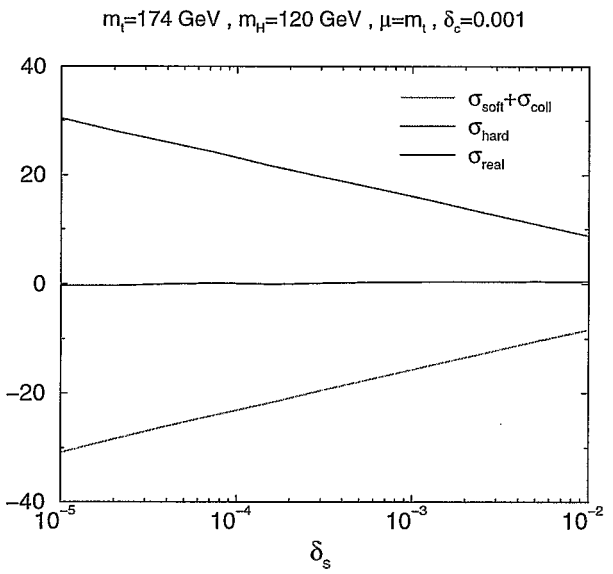

Figure 21. NLO QCD corrections to $p\overline{p} \to t\bar{t}h$ at $\sqrt{S} = 2\ TeV$. This figure shows the independence of the total cross section on the soft cutoff, δ_s.[34]

- σ_{soft}: This contains the soft singularities arising from both the initial and final state soft gluon radiation in the limit $p_g \to 0$. The calculation is analogous to the discussion of Section 4.3.
- σ_{hard} : This is the contribution from real gluon radiation when the gluon has an energy above the soft cut-off. In contrast to the e^+e^- example of Section 4.3, this contribution has a singularity when the initial state quark or gluon is parallel to the radiated final state gluon. The initial state collinear singularities are absorbed into the parton distribution functions (PDFs).

The combination $\sigma_{soft} + \sigma_{hard} + \sigma_{virtual}$ is finite.

4.8. *Collinear Singularities and Phase Space Slicing*

To illustrate the effects of collinear singularities, we consider the parton level subprocess,

$$q(p) + \overline{q}(q) \to t(p_t) + \overline{t}(p_{t'}) + h(p_h) + g(p_g)\ . \tag{109}$$

As in the e^+e^- example, we divide the gluon phase space into a soft and a hard region. We then further divide σ_{hard} into a region with collinear

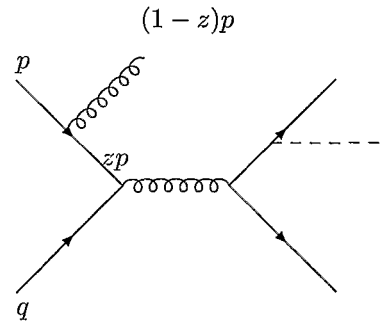

Figure 22. Diagram contributing to collinear singularity for the process $q\bar{q} \to t\bar{t}hg$.

divergences and a finite region,

$$\sigma_{hard} \equiv \sigma_{hard}\,|_{coll} + \sigma_{hard}\,|_{not-coll} \tag{110}$$

The separation depends on a new cut-off, δ_c, although σ_{hard} must be independent of δ_c. If the emitted gluon is from the initial state quark line, then there is a quark propagator,

$$\frac{1}{(p-p_g)^2} = -\frac{1}{2p\cdot p_g} = -\frac{1}{\sqrt{s}E_g(1-\cos\theta)} \tag{111}$$

which becomes singular when p and p_g are parallel ($\cos\theta \to 1$). The hard/not-collinear region is defined by,

$$\frac{2p\cdot p_g}{E_g\sqrt{s}} > \delta_c \qquad \frac{2q\cdot p_g}{E_g\sqrt{s}} > \delta_c\ . \tag{112}$$

In this region the quark propagator of Eq. 111 is finite and the cross section can be computed numerically.

In the collinear region,

$$\frac{2p\cdot p_g}{E_g\sqrt{s}} < \delta_c \qquad \frac{2q\cdot p_g}{E_g\sqrt{s}} < \delta_c, \tag{113}$$

and the matrix element factorizes into a parton i splitting into a hard parton i' plus a collinear gluon with kinematics

$$\begin{aligned} p_{i'} &= zp_i \\ p_g &= (1-z)p_i \\ s_{ig} &\equiv 2p_i\cdot p_g \end{aligned}$$

These kinematics are illustrated in Fig. 22. In the current example, $q \to qg$ and the matrix element factorizes,[34]

$$|\,A(ij \to t\bar{t}h+g)\,|^2 \to_{collinear} \Sigma_{i'} g_s^2\,|\,A_{LO}(i'j \to t\bar{t}h)\,|^2\,\frac{2P_{ii'}(z)}{zs_{ig}} \tag{114}$$

where $P_{ii'}$ is the probability that parton i splits into parton i', with fraction z of the initial momentum. In this example,

$$P_{ii'}(z) = P_{qq}(z) = C_F\left[\frac{1+z^2}{1-z} - \epsilon(1-z)\right] . \tag{115}$$

The phase space also factorizes in the collinear limit:[31]

$$(PS)_4(ij \to t\bar{t}h + g)_{collinear} \to (PS)_3(i'j \to t\bar{t}h)\frac{\Gamma(1-\epsilon)}{\Gamma(1-2\epsilon)}\frac{(4\pi)^\epsilon}{16\pi^2}$$
$$\cdot z\, dz\, ds_{ig}[(1-z)s_{ig}]^{-\epsilon}\theta\left(\frac{(1-z)}{z}p_{i'}\cdot p_j\delta_c - s_{ig}\right) \tag{116}$$

Combining Eqs. 115 and 116, the hard-collinear parton level cross section becomes:[45]

$$\sigma_{hard/coll} = \frac{\alpha_s}{2\pi}\frac{\Gamma(1-\epsilon)}{\Gamma(1-2\epsilon)}\left(\frac{4\pi\mu^2}{M_t^2}\right)^\epsilon\left(-\frac{1}{\epsilon}\right)\delta_c^{-\epsilon}$$
$$\cdot\Sigma_{i'}\left\{\int_0^{1-\delta_s} dz\left[\frac{(1-z)^2 p_{i'}\cdot p_j}{zM_t^2}\right]^{-\epsilon} P_{ii'}(z)\sigma_{LO}(i'j \to t\bar{t}h)\right.$$
$$\left. + (i \leftrightarrow j)\right\} . \tag{117}$$

This result has a dependence on both δ_c and δ_s. The $1-\delta_s$ limit on the z integration excludes soft gluon region. The remaining singularities in Eq. 117 are absorbed into the mass factorization as described in the next section.

4.9. *Mass Factorization*

The hadronic cross section depends on the PDFs, $f_i(x)$:

$$\sigma_H(S) = \Sigma_{ij}\int f_i(x_1)f_j(x_2)\hat{\sigma}_{ij}(x_1x_2S)dx_1dx_2 ,$$

where $\hat{\sigma}$ is the parton level cross section. At lowest order, there is no dependence on the renormalization/ factorization scale, μ. Since the only physical quantity is the hadronic cross section, $\sigma_H(S)$, we can define scale dependent PDFs to absorb the hard/collinear singularity of Eq. 117,[30,31]

$$f_i(x,\mu) \equiv f_i(x) + \left(-\frac{1}{\epsilon}\right)\frac{\alpha_s}{2\pi}\frac{\Gamma(1-\epsilon)}{\Gamma(1-2\epsilon)}\left(\frac{4\pi\mu^2}{\mu^2}\right)^\epsilon$$
$$\cdot\left\{\int_z^{1-\delta_s}\frac{dz}{z}P_{ii'}(z)f_{i'}(\frac{x}{z}) + C_F(2\log(\delta_s) + \frac{3}{2})\right\} . \tag{118}$$

The upper limit on the z integration excludes the soft region. After convoluting the parton cross section with the renormalized quark distribution function of Eq. (118), the infrared singular counterterm of Eq. (118) exactly cancels the remaining infrared poles of $\hat{\sigma}_{virt} + \hat{\sigma}_{soft} + \hat{\sigma}_{hard/coll}$.

The cancellation of the cutoff dependence at the level of the total NLO cross section is a very delicate issue, since it involves both analytical and numerical contributions. It is crucial to study the behavior of σ_{NLO} in a region where the cutoff(s) are small enough to justify the approximations used in the analytical calculation of the infra-red divergent soft and collinear limits, but not so small to give origin to numerical instabilities. This effect is illustrated in Fig. 21.

The NLO result for $p\bar{p} \to t\bar{t}h$ at the Tevatron is shown in Fig. 23 as a function of the unphysical factorization/ renormalization scale. The complete calculation includes not only the $q\bar{q}$ initial state described here, but also the gg and qg initial states. Note the reduced μ dependence of the NLO rate from the lowest order prediction. The cross section is very small, making this a challenging measurement.

At the LHC, the process $pp \to t\bar{t}h$ has a significant rate for $M_h < 130\ GeV$ and we can look for $h \to b\bar{b}$, giving the final state of $W^+W^-b\bar{b}b\bar{b}$. This is an important discovery channel for a Higgs with $M_h < 130\ GeV$. The ATLAS experiment, with $L = 100\ fb^{-1}$, and assuming $M_h = 120\ GeV$ can measure $\frac{\delta g_{tth}}{g_{tth}} \sim 16\%$. This is illustrated in Fig. 24.[26] The signal and the background have similar shapes at the LHC, increasing the difficulty of this measurement.

5. Heavy Top as Inspiration for Model Builders

We turn now to a discussion of the top quark in models where there is new physics involving the top quark beyond that of the Standard Model. The fact that the top quark is much heavier than the other quarks gives it a special role in electroweak symmetry breaking. In this section, we examine the role of the top quark in the minimal supersymmetric model and in models with dynamical symmetry breaking. We pay particular attention to how data from the Tevatron and the LHC can help us to test these ideas.

The large value of the top quark mass has important consequences in a supersymmetric (SUSY) model.[46] In the SM, the Higgs boson mass is a free parameter, while in a SUSY model there is an upper limit on the Higgs mass. At tree level in the minimal SUSY model, $M_h < M_Z$, but the large

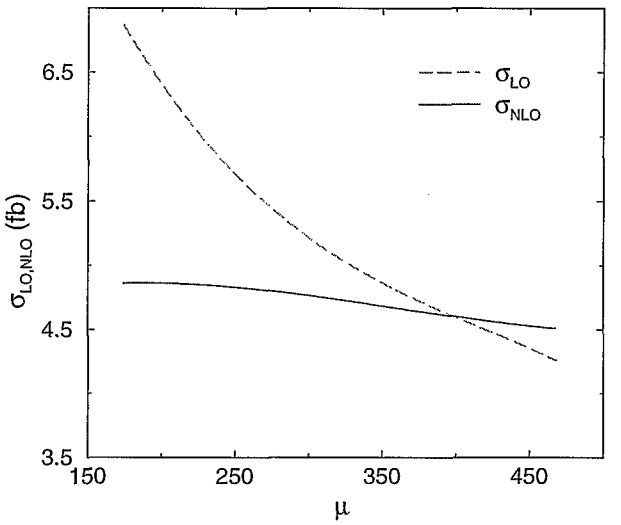

Figure 23. Leading order and next-to-leading order rate for $p\bar{p} \to t\bar{t}h$ at the Tevatron for $M_h = 120\ GeV$ and $\sqrt{S} = 2\ TeV$ as a function of the unphysical factorization/renormalization scale.[34]

top quark mass, and the subsequent large coupling to the Higgs boson,

$$\frac{m_t\sqrt{2}}{v} \sim 1, \tag{119}$$

lead to large radiative corrections to the prediction for the Higgs boson mass, raising the lower limit on the Higgs mass significantly. In addition, corrections due to the large top quark mass typically imply that the scalar partner of the top, the stop, is the lightest squark.

A further difference between the SM and a SUSY model which is due to the large top quark mass is the understanding of the mechanism of electroweak symmetry breaking in a SUSY model. If the supersymmetric model is embedded in a grand unified model, then the simplest version (mSUGRA) has the interesting property that the evolution of the parameters from the

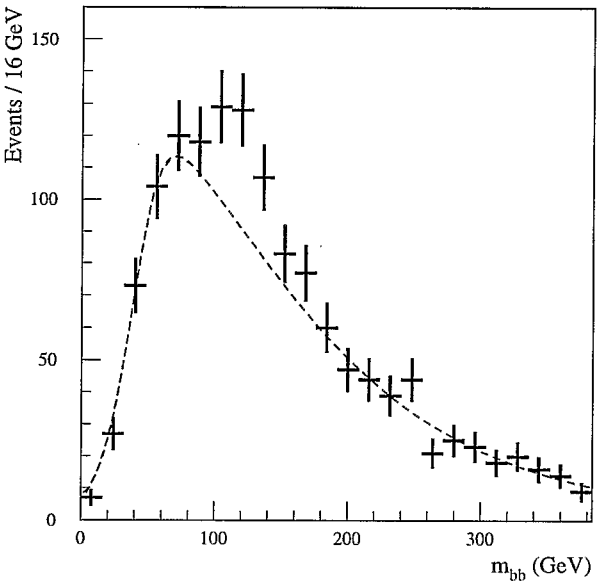

Figure 24. Invariant mass for the $b\bar{b}$ pair from the Higgs decay in the process $pp \to t\bar{t}h$ at the LHC with $M_h = 120\ GeV$ (data points). The dashed line is the background. The error bars correspond to the statistical uncertainty with an integrated luminosity of $L = 100\ fb^{-1}$.[26]

GUT scale to the weak scale drives the Higgs mass-squared negative as a consequence of the large value of M_t, and therefore explains electroweak symmetry breaking. In fact, this mechanism *requires* that the top quark have a mass near its observed value.

In models with dynamical symmetry breaking, the large value of the top quark mass can imply that the top quark is different from the lighter quarks, perhaps having different gauge interactions in an extended gauge sector. In Section 5.6, we discuss topcolor as an example of a model of dynamical symmetry breaking where the top quark plays a special role. Many possibilities for dynamical symmetry breaking in electroweak interactions are detailed in the review by Hill and Simmons.[47]

5.1. *EWSB and the top quark mass*

We begin by considering the importance of the top quark mass in the SM. In the SM, electroweak symmetry breaking occurs through the interactions of an $SU(2)_L$ doublet scalar field, Φ, with a scalar potential,[48]

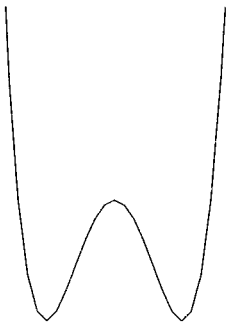

Figure 25. Higgs potential in the Standard Model with $\mu^2 < 0$.

$$V = \mu^2 \Phi\Phi^\dagger + \lambda(\Phi\Phi^\dagger)^2 \quad . \tag{120}$$

If $\mu^2 < 0$, the neutral component of the Higgs doublet gets a vacuum expectation value,

$$\langle \Phi_0 \rangle = \frac{v}{\sqrt{2}} \tag{121}$$

and the scalar potential has the shape shown in Fig. 25. Electroweak symmetry breaking (EWSB) occurs and masses are generated for the W and Z gauge bosons. After EWSB, there remains in the spectrum a physical particle, the Higgs boson, h, and at tree level the quartic self- coupling of the Higgs boson, λ, is related to the Higgs mass by

$$M_h^2 = 2\lambda v^2. \tag{122}$$

A measurement of this relationship would test the mechanism of EWSB.

Eq. 120 is the scalar potential at the electroweak scale, $\Lambda \sim v$. All parameters of the electroweak theory change with the energy scale Λ in a precisely calculable way, and so will be different at higher energies. The most interesting parameters for us are the Higgs quartic self-coupling, λ,

and the top quark Yukawa coupling, $g_{tth} = \frac{M_t}{v}$. To one loop accuracy,[c]

$$\Lambda\frac{d\lambda}{d\Lambda} = \frac{1}{16\pi^2}\left[24\lambda^2 - (A - 12g_{tth}^2)\lambda + B - 12g_{tth}^4\right]$$
$$\Lambda\frac{dg_{tth}}{d\Lambda} = \frac{1}{16\pi^2}\left(\frac{g_{tth}}{12}\right)\left[54g_{tth}^2 - 17g'^2 - 27g'^2 - 96g_s^2\right] \qquad (123)$$

where,

$$A = 3(3g^2 + g'^2)$$
$$B = \frac{3}{8}\left(2g^4 + (g^2 + g'^2)^2\right). \qquad (124)$$

We have omitted the equations for the running of the gauge coupling constants. They can be found in Ref. 48.

In order for electroweak symmetry breaking to occur, the quartic coupling must remain finite at all scales,

$$\frac{1}{\lambda(\Lambda)} > 0. \qquad (125)$$

As λ is evolved from the weak scale to higher energy, it grows and eventually becomes infinite at some large scale. When λ becomes large, the scaling of Eq. 124 can be approximated,

$$\Lambda\frac{d\lambda}{d\Lambda} = \frac{3}{2\pi^2}\lambda^2 \, . \qquad (126)$$

Eq. 126 is easily solved,

$$\frac{1}{\lambda(\Lambda)} = \frac{1}{\lambda(M_h)} - \frac{3}{2\pi^2}\log\left(\frac{\Lambda}{M_h}\right) \, . \qquad (127)$$

The position where $\lambda(\Lambda) \to \infty$ is known as the Landau Pole. Since λ is related to the Higgs mass, $M_h^2 = 2v^2\lambda$, the requirement that the theory not approach the Landau pole gives an upper bound on the Higgs boson mass,

$$M_h^2 < \frac{4\pi^2 v^2}{3\log\left(\Lambda/M_h\right)} \, . \qquad (128)$$

This means that at the scale Λ there must be some new physics beyond that of the SM which enters. The SM simply makes no sense at energy scales larger than Λ since in this region the Higgs quartic self-coupling is

[c] g and g' are the $SU(2)_L$ and $U(1)_Y$ gauge coupling constants.

infinite. Assuming no new physics before the GUT scale, $\Lambda \sim 10^{16}\ GeV$, gives a bound on the Higgs mass of[49,50]

$$M_h < 160\ GeV\ . \tag{129}$$

This bound corresponds to the upper curve in Fig. 26. Non-perturbative studies using lattice gauge theory confirm the validity of this limit.[51]

Conversely, we require that the potential be bounded from below, which is equivalent to the restriction that $\lambda > 0$ at large Φ. The scaling of the quartic coupling near $\lambda = 0$ is,

$$\Lambda \frac{d\lambda}{d\Lambda} = \frac{1}{16\pi^2}\left[B - 12 g_{tth}^4\right] \tag{130}$$

which can be solved,

$$\lambda(\Lambda) = \lambda(M_h) + \frac{B - 12 g_{tth}^4}{16\pi^2} \log\left(\frac{\Lambda}{M_h}\right)\ . \tag{131}$$

The requirement that $\lambda(\Lambda) > 0$ gives a lower bound on the Higgs mass,

$$\frac{M_h^2}{2v^2} > \frac{12 g_{tth}^4 - B}{16\pi^2} \log\left(\frac{\Lambda}{M_h}\right)\ . \tag{132}$$

A complete approach must include the full set of renormalization group equations, including the running of the coupling constants for large values of Φ.

The restrictions on the Higgs mass from consistency of the theory are shown in Fig. 26, where the allowed region for a scale Λ is the area between the curves, known as the "chimney". At a given scale Λ, the Higgs mass has a lower limit from bounding the potential from below and an upper limit from the requirement that Higgs quartic coupling, λ, be finite. The exact shape of the allowed region depends sensitively on the value of M_t.[49,50]

The SM with a Higgs mass in the 130 GeV region is consistent at energy scales all the way to the Planck scale. The theory is still unsatisfactory however, because it provides no explanation of why $\mu^2 < 0$, as required for EWSB. In addition, the Higgs mass is a free parameter in the SM and there is no understanding of why it should have any particular value. In the next section, we will see that low energy supersymmetry can potentially solve both these problems.

5.2. *Supersymmetry and the Top Quark*

TeV scale supersymmetric models explain several mysteries about the SM:

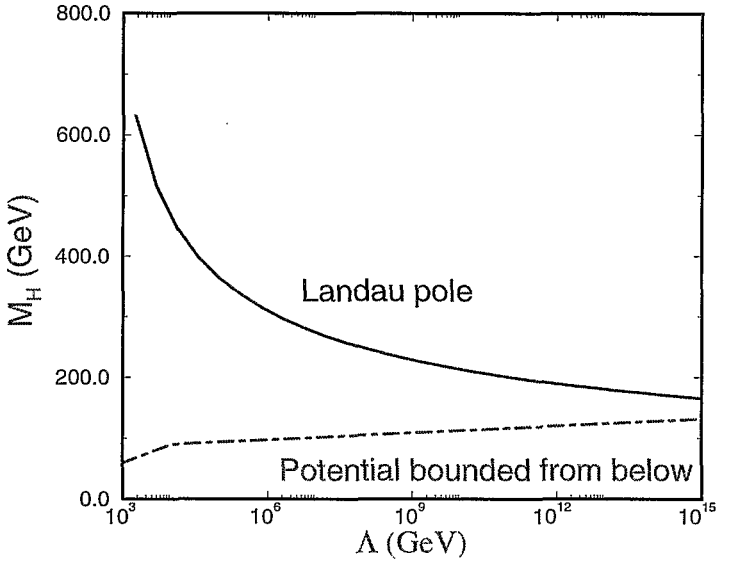

Figure 26. Limits on the Higgs boson mass as a function of the cutoff scale Λ. The theoretically consistent region lies between the two curves.[49]

- A heavy top quark and mSUGRA (minimal supergravity) explain why $\mu^2 < 0$.
- A heavy top quark and the MSSM (minimal supersymmetric Standard Model) explain why the Higgs mass may light, as suggested by precision measurements.

In this section, we give a brief review of phenomenological models of supersymmetry and discuss the relationship between the top quark mass and the requirement that supersymmetry exist below the TeV scale.

Supersymmetry is a symmetry which relates the masses and couplings of particles of differing spin. To each SM chiral fermion is associated a complex scalar and each of the $SU(3) \times SU(2)_L \times U(1)_Y$ gauge bosons similarly acquires a Majorana fermion partner. Supersymmetry connects particles of differing spin, but with all other characteristics the same.[52] In an unbroken supersymmetric model, particles and their superpartners have identical masses. It is clear, then, that **supersymmetry must be a broken symmetry** if it is to be a theory of low energy interactions. There is no scalar particle, for example, with the mass and quantum numbers of the electron. In fact, there are no candidate supersymmetric scalar partners for any of the fermions in the experimentally observed spectrum. The most general soft breaking of supersymmetry introduces masses and mixing parameters and the theory loses much of its capabilities for specific predictions.

The Higgs sector in a SUSY model always contains at least two $SU(2)_L$ doublets. In the supersymmetric extension of the Standard Model, the Higgs doublet acquires a SUSY partner which is an $SU(2)_L$ doublet of Majorana fermion fields, $\tilde{h}_1$ (the Higgsinos), which contribute to the triangle $SU(2)_L$ and $U(1)_Y$ gauge anomalies as described in Section 2.1. Since the fermions of the Standard Model have exactly the right quantum numbers to cancel these anomalies, it follows that the contribution from the fermionic partner of the Higgs doublet remains uncancelled.[6,7] This contribution must be cancelled by adding a second Higgs doublet (and its Majorana fermion partner) with precisely the opposite $U(1)_Y$ quantum numbers from the first Higgs doublet.

All supersymmetric models thus have at least 2-Higgs doublets and so the minimal supersymmetric model has 5 physical Higgs bosons: $h^0, H^0, A^0, H^{\pm}$. The ratio of the vacuum expectation values of the neutral Higgs bosons,

$$\tan\beta \equiv \frac{v_2}{v_1} \tag{133}$$

is a fundamental parameter of the theory. At tree level, the neutral Higgs boson masses are predicted in terms of two parameters, which are usually taken to be $\tan\beta$ and the mass of the pseudoscalar Higgs boson, M_A. The neutral Higgs boson masses are then predicted,

$$M^2_{h,H} = \frac{1}{2}(M_A^2 + M_Z^2) \mp \frac{1}{2}\sqrt{(M_A^2 + M_Z^2)^2 - 4M_Z^2 M_A^2 \cos^2 2\beta} \tag{134}$$

which gives an upper bound on the lightest Higgs mass:

$$M_h < M_Z \mid \cos 2\beta \mid < M_Z \tag{135}$$

which is excluded experimentally. (In a SUSY model, the LEP and LEPII results require $M_h > 89.8\ GeV$.[4])

The Higgs mass prediction in a supersymmetric model receives large radiative corrections from top and stop squark loops. At 1-loop, and neglecting possible soft SUSY breaking tri-linear scalar mixing, the lightest Higgs mass becomes:

$$M_h^2 = \frac{M_A^2 + M_Z^2 + \epsilon}{2} - \frac{1}{2}\Big\{(M_A^2 + M_Z^2 + \epsilon)^2 - 4M_Z^2 M_A^2 \cos^2 2\beta$$
$$-4\epsilon(M_A^2 \sin^2\beta + M_Z^2 \cos^2\beta)\Big\}^{1/2} \tag{136}$$

where,

$$\epsilon = \frac{3G_F}{\sqrt{2}\pi^2}\frac{M_t^4}{\sin^2\beta}\log\left(\frac{\tilde{M}_t^2}{M_t^2}\right), \tag{137}$$

and $\tilde{M}_t$ is the average stop squark mass. For unbroken supersymmetry, the top and stop have the same masses, $M_t = \tilde{M}_t$, and the bound of Eq. 135 is recovered. The mass splitting between the top and stop in a broken SUSY theory changes the upper bound on the Higgs mass to,

$$M_h^2 < M_Z^2 \cos^2 2\beta + \epsilon \sin^2\beta. \tag{138}$$

The large M_t^4 corrections raise the Higgs mass bound above the experimental limit, as shown in Fig. 27.

There are many analyses[53] which include a variety of two-loop effects, renormalization group effects, etc., but the important point is that for given values of $\tan\beta$, the scalar mixing parameters, and the squark masses, there is an upper bound on the lightest neutral Higgs boson mass. For large values of $\tan\beta$ the limit is relatively insensitive to the value of $\tan\beta$ and with a squark mass less than about 1 TeV, the upper limit on the Higgs mass is about 110 GeV if mixing in the top squark sector is negligible. For large mixing, this limit is raised to around 130 GeV.

5.3. *mSUGRA*

The minimal supersymmetric model (MSSM) is constructed by adding to the Lagrangian all of the soft supersymmetry breaking terms allowed by the gauge symmetries. These include masses for all the new SUSY particles and tri-linear scalar mixing terms. The most general Lagrangian of this type has 105 new parameters beyond those of the Standard Model. In order to make definite predictions, the simplifying assumption that the soft

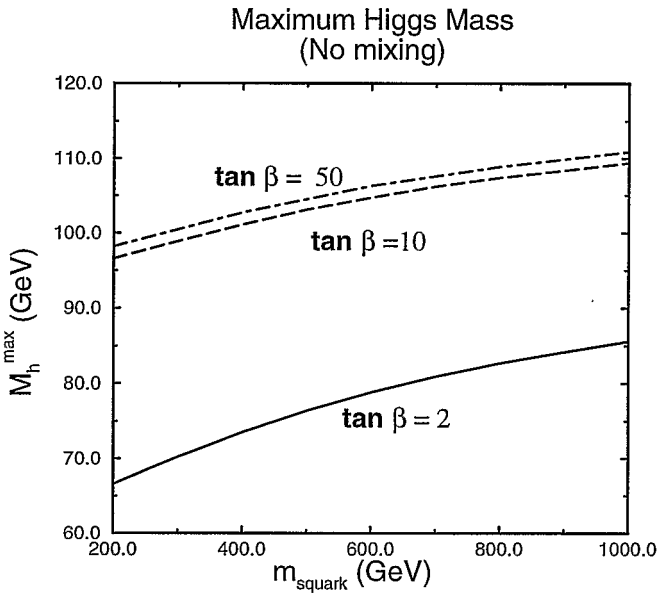

Figure 27. Upper bound on Higgs mass in MSSM at one loop and with no soft trilinear mixing.[53]

parameters unify at M_{GUT} is often made. (The resulting model is usually called mSUGRA or the CMSSM). In this framework the model is completely specified by five parameters:

- Common scalar mass at M_{GUT}, $\tilde{m}_0$
- Common gaugino mass at M_{GUT}, $M_{1/2}$
- 1 Higgs mass-squared, m_{12}^2
- 1 tri-linear coupling at M_{GUT}, $A_0\lambda_F$
- sign($\hat{\mu}$)

The parameter $\hat{\mu}$ describes the mixing between the two Higgs doublets. At the GUT scale, the Higgs masses are,

$$M^2_{h,H}(M_{GUT}) = m_0^2 + \hat{\mu}^2, \tag{139}$$

while the squark and slepton masses are

$$M^2_{\tilde{q}}(M_{GUT}) = M^2_{\tilde{l}}(M_{GUT}) = m_0^2 \ . \tag{140}$$

The theory must explain why the lightest neutral Higgs mass-squared becomes negative at the weak scale and breaks the electroweak symmetry, while the scalar fermion masses remain positive so as to not break color and electromagnetism.

In an mSUGRA model, the masses and parameters are evolved using the renormalization group equations (RGE) to scale from M_{GUT} down to the weak scale in order to make predictions for the masses at the weak scale. The large top quark mass plays an important role here. We can understand the basic scaling by considering only the Higgs doublet, H_2,[d] the scalar partners of the third generation $SU(2)_L$ fermion doublet, $(\tilde{t}_L, \tilde{b}_L) \equiv \tilde{Q}_3$, and the scalar partner of the right-handed top quark, $\tilde{t}_R$. The renormalization group scaling is given by:[54]

$$\frac{dM^2_{H_2}}{d\log(\Lambda)} = \frac{1}{8\pi^2}(3g^2_{ttH}X_t - 3g^2M_2^2 - g'^2M_1^2)$$

$$\frac{d\tilde{M}^2_{t_R}}{d\log(\Lambda)} = \frac{1}{8\pi^2}(2g^2_{ttH}X_t - \frac{16}{3}g_s^2M_3^2 - \frac{16}{9}g'^2M_1^2)$$

$$\frac{d\tilde{M}^2_{Q_3}}{d\log(\Lambda)} = \frac{1}{8\pi^2}(g^2_{ttH}X_t - \frac{16}{3}g_s^2M_3^2 - 3g^2M_2^2 - \frac{1}{9}g'^2M_1^2)$$

where,

$$X_t \equiv M^2_{H_2} + \tilde{M}^2_{Q_3} + \tilde{M}^2_{t_R} + A_t^2 \ . \tag{141}$$

$M_{3,2,1}$ are the gaugino masses associated with the $SU(3) \times SU(2)_L \times U(1)_Y$ gauge sector, g_{ttH} is the coupling of the Higgs to the top quark in the MSSM, and A_t is the soft SUSY mixing term in the top sector. The QCD term (proportional to g_s^2) makes $\tilde{M}^2_{t_R}, \tilde{M}^2_{Q_3}$ increase faster than M_{H_2} as the scale is reduced from M_{GUT}. The Yukawa term (proportional to g_{ttH}) drives $M^2_{H_2} < 0$, while the other scalar mass-squared terms remain positive. This behavior is a consequence of the large M_t value.

[d] H_2 is the $SU(2)_L$ doublet with isospin $Y = +\frac{1}{2}$.

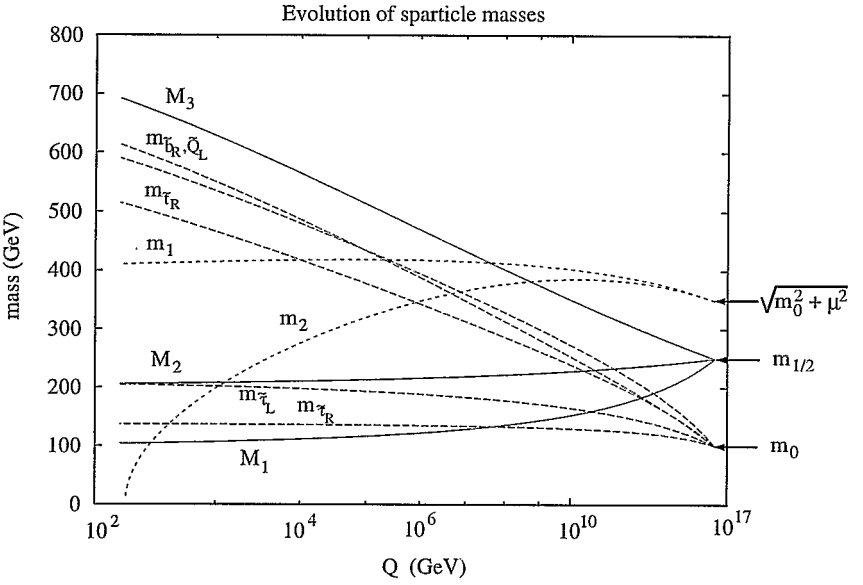

Figure 28. Typical pattern of masses in an mSUGRA model.[55].

Neglecting the gauge couplings, we have:

$$\frac{d}{d\log(\Lambda)}\begin{pmatrix} M_{H_2}^2 \\ \tilde{M}_{tR}^2 \\ \tilde{M}_{Q_3}^2 \end{pmatrix} = \frac{g_{tth}^2}{8\pi^2} X_t \begin{pmatrix} 3 \\ 2 \\ 1 \end{pmatrix} , \tag{142}$$

which can be easily solved,

$$M_h^2(\Lambda) = M_h^2(M_{GUT}) - \frac{3g_{tth}^2}{8\pi^2} X_t \log(\frac{M_{GUT}}{\Lambda}) . \tag{143}$$

For heavy M_t, M_h^2 becomes negative and triggers EWSB. It is interesting that this behavior *requires* $M_t \sim 175\ GeV$.[55]

The RGE scaling from the GUT scale to the weak scale in mSUGRA type models yields a a typical pattern of masses, as seen in Fig. 28. The gluino is the heaviest gaugino, while the squarks are significantly heavier than the sleptons.

5.4. *Charged Higgs Decays*

The pattern of top quark decays is changed in the MSSM from that of the SM, due to the extended Higgs sector. The presence of a charged Higgs

boson allows the decay, $t \to H^+ b$ if the mass of the charged Higgs is less than $M_t - m_b$. This decay looks similar to $t \to Wb$ and can have a significant rate. The coupling of the charged Higgs to the t b system is,

$$g_{tH^+b} \sim m_t \cot\beta P_+ + m_b \tan\beta P_- \tag{144}$$

and so this decay is relevant both for very large and for very small $\tan\beta$. For small $\tan\beta$, $H^+ \to cs$ and $H^+ \to t^* b$, while for large $\tan\beta$, $H^+ \to \tau\nu$. These decays would suppress the rate for top decays to leptons plus jets in the SM top search. In Run I, the Tevatron experiments placed a limit on M_{H^+} of roughly $M_{H^+} > 100\ GeV$ for $\tan\beta < 1$ or $\tan\beta > 50$.[56]

5.5. *The Top squark*

The mass-squared matrix for the scalar partners of the left and right handed top quarks $(\tilde{t}_L, \tilde{t}_R)$ includes mixing between the partners of the left- and right- handed top:

$$\tilde{M}_t^2 = \begin{pmatrix} \tilde{M}_{Q_3}^2 + M_t^2 + M_Z^2 L_t \cos 2\beta & M_t(A_t - \hat{\mu}\cot\beta) \\ M_t(A_t - \hat{\mu}\cot\beta) & \tilde{M}_{t_R}^2 + M_t^2 + M_Z^2 R_t \cos 2\beta \end{pmatrix}$$

The mixing is proportional to the top quark mass and so the large value of M_t can cause one of the top squarks to be relatively light. If the scalar mass scale, $\tilde{M}_{Q_3}$ is much larger than M_Z, M_t, A_t, then the stop masses are roughly degenerate $\sim \tilde{M}_{Q_3}$. On the other hand if $\tilde{M}_{Q_3} \sim M_Z, M_t, A_t$, then the large mixing effects drive the stop mass to a small value and the stop squark becomes the lightest squark.

It is possible to search for a light stop in the decays of the top, $t \to \tilde{t}\tilde{\chi}^0$, where $\tilde{\chi}^0$ is the lightest neutral SUSY particle. The limits then depend on the assumed branching ratio for the top into stop decays. The Run I data was sensitive to stop and chargino masses in the 100 GeV range.[57]

5.6. *The Top Quark and Dynamical Symmetry Breaking*

The top quark has a special role in technicolor models where a $t\bar{t}$ condensate can play the part of the Higgs boson in generating EWSB. This can happen in models where there is a new strong interaction felt by the top quark, but not by the lighter quarks. The proto-type model of this type is called *topcolor*.[?] A review of this class of models can be found in Ref.

[47]. Topcolor models are constructed by expanding the strong gauge group from the $SU(3)$ of QCD to,

$$SU(3)_{tc} \times SU(3) \rightarrow SU(3)_{QCD} \tag{145}$$

$SU(3)_{tc}$ couples only to the 3rd generation with a coupling g_{tc}, while the second $SU(3)$ gauge symmetry couples only to the first two generations. The symmetry is broken to $SU(3)_{QCD}$ at a scale M. Below M, the gauge bosons of the $SU(3)_{tc}$ group, the "topgluons", are massive and lead to effective 4-Fermi interactions between the top quarks:

$$L \sim \frac{g_{tc}^2}{M^2}(\overline{Q}_{3L}\gamma_\mu \frac{T^A}{2} Q_{3L})(\bar{t}_R \gamma^\mu \frac{T^A}{2} t_R), \tag{146}$$

where T^A is the $SU(3)$ generator in the adjoint representation and Q_{3L} is the left-handed (t_L, b_L) doublet. If the $SU(3)_{tc}$ coupling, g_{tc}, is larger than a critical value, a top condensate forms, $\langle \bar{t}t \rangle$, which breaks the electroweak symmetry and generates a mass for the top quark. One must arrange that $\langle \bar{t}t \rangle \neq 0$ and $\langle \bar{b}b \rangle = 0$. This is usually done by adding an additional $U(1)_h$ gauge symmetry under which the t and b quarks transform differently.

This class of models can be tested at the Tevatron and the LHC by searching for effects of the top gluons and the new Z', and through B decays.[59] Since the Z' boson corresponding to the $U(1)_h$ and the top gluons of $SU(3)_{tc}$ couple differently to the third generation and to the lighter quarks, they lead to flavor changing neutral currents. Present limits from B meson mixing require that the topgluon be heavier than $3-5\ TeV$ and $M_{Z'} > 7-10\ GeV$.[58]

6. Conclusions

The story of the top quark is far from over. Its properties and its role in the SM and in physics beyond the SM will be further elucidated in the emerging Run II data at the Tevatron. The increased statistics of Run II will enable more precise measurements of the mass, couplings, and decay properties of the top. The LHC will provide even more insight into the role of the top quark. It is possible that surprises are just around the corner!

Acknowledgements

I would like to thank K.T. Mohanthapa, H. Haber, and A. Nelson for organizing such an enjoyable and successful school.

References

1. T. Abe . *et. al.*, *Phys. Rev. Lett.* **74** (1995) 2626, *Phys. Rev.* **D50** (1994) 2966; S. Abachi *et. al.*, *Phys. Rev. Lett.* **74** (1995) 2632, hep-ex/9503003.
2. F. Abe *et. al.*, *Phys. Rev. Lett.* **82** (1999) 271, hep-ex/9810029; S. Abachi *et. al.*, *Phys. Rev.* **D60** (1999) 052001.
3. See results of LEP Electroweak Working Group, http://lepewwg.web.cern.ch/LEPEWWG/.
4. Particle Data Group, K. Hagiwara *et. al.*, *Phys. Rev.* **D66** (2002) 010001.
5. E. Simmons, TASI2000, hep-ph/0011244; S. Willenbrock, *Rev. Mod. Phys.* **72** (2000) 1141, hep-ph/0211067; hep-ph/0008189.
6. M. Peskin and D.Schroeder, *An Introduction to Quantum Field Theory*, (Addison-Wesley, Reading, 1995).
7. C. Quigg, *Gauge Theories of the Strong, Weak, and Electromagnetic Interactions*, (Benjamin-Cummings, Reading, 1983).
8. E. Rice *et. al.*, *Phys. Rev. Lett.* **48** (1982) 906.
9. J. Kuhn, *The Top Quark and The Electroweak Interaction*, 1995 SLAC Summer School, hep-ph/9707321.
10. G. Degrassi and A. Sirlin, *Nucl. Phys.* **B352** (1991) 342.
11. M. Carena *et. al.*, Report of the Tevatron Higgs Working Group, hep-ph/0010338.
12. P. Nason, S. Dawson, and R. K. Ellis, *Nucl. Phys.* **B303** (1988) 607.
13. W. Beenakker, H. Huijf, W. van Neerven, and J. Smith, *Phys. Rev.* **D40** (1989) 54.
14. S. Catani *et. al.*, *Phys. Lett.* **B378** (1996) 329, hep-ph/9602208; E. Berger and H. Contopanagos, *Phys. Lett.* **B361** (1995) 115, hep-ph/9507363; E. Laenen, J. Smith, and W. van Neerven, *Nucl. Phys.* **B369** (1992) 543; R. Bonciani, S. Catani, M. Mangano, and P. Nason, *Nucl. Phys.* **B529** (1998) 424, hep-ph/9801375.
15. M. Cacciari *et. al.*, hep-ph/0303085.
16. F. Abe *et. al.*, *Phys. Rev. Lett.* **80** (1998) 2773, hep-ph/971008; S. Abachi *et. al.*, *Phys. Rev. Lett.* **79** (1997) 1203; hep-ex/9703008.
17. T. Affolder *et.al.*, *Phys. Rev. Lett.* **86** (2001) 3233, hep-ph/0012029.
18. G. Eilam *et.al.*, *Phys. Rev. Lett.*, **66** (1991) 3105; T. Mehen, *Phys. Lett.* **B417** (1998) 353, hep-ph/9707365.
19. T. Affolder *et. al.*, *Phys. Rev. Lett.* **84** (2000) 216, hep-ph/9909042.
20. D. Amidei and R. Brock, *Tev 2000 Study* (1996), FERMILAB-Pub-96/082.
21. J. Womersley, TASI02, Boulder, Colorado, hep-ex/0301007; D. Chakraborty, J. Konigsberg, and D. Rainwater, hep-ph/0303092.
22. F. Abe *et. al.*, *Phys. Rev. Lett.* **80** (1998) 2767, hep-ex/9801014; S. Abachi *et. al.*, *Phys. Rev. Lett.* **79** (1997) 1197, hep-ex/9703008.
23. M. Smith and W. Willenbrock, *Phys. Rev.* **D54** (1996) 6696, hep-ph/9604223; S. Zhu, *Phys. Lett.* **B524** (2002) 238, hep-ph/0109269.
24. T. Stelzer, Z. Sullivan, and S. Willenbrock, *Phys. Rev.* **D56** (1997) 5919, hep-ph/9705398.
25. U. Baur *et. al.*, Snowmass 2001, Snowmass, Colorado, hep-ph/0202001.

26. M. Beneke *et. al.*, LHC Top Study, hep-ph/0003033.
27. G. Mahlon and S. Parke, *Phys. Lett.* **B411** (1997) 173, hep-ph/9706304; V. Barger, J. Ohnemus, and R. Phillips, *Int. J. Mod. Phys.* **A4** (1989) 617.
28. J. Jersak, E. Laermann and P. Zerwas, *Phys. Rev.* **D25** (1982) 1218; V. Ravindran and W. van Neerven, *Phys. Lett.* **B445** (1998) 214, hep-ph/9809411.
29. H. Baer, J. Ohnemus, and J. Owens, *Phys. Rev* **D40** (1989) 2844.
30. B. Harris and J. Owens, *Phys. Rev.* **D65** (094032) , hep-ph/0102128.
31. W. Giele and N. Glover, *Phys. Rev.* **D46** (1992) 1980; W. Giele, N. Glover, and D. Kosower, *Nucl. Phys.* **B403** (1993) 633, hep-ph/9302225.
32. G. Sterman, *Introduction to Quantum Field Theory* (Cambridge University Press, Cambridge, 1993).
33. G. Grammer and D. Yennie, *Phys. Rev.* **D8** (1973) 4332; F. Fiorani, G. Marchesini, and L. Reina, *Nucl. Phys.* **B309** (1988) 439.
34. L. Reina, S. Dawson, and D. Wackeroth, *Phys. Rev.* **D65** (2002) 053017, hep-ph/0109066.
35. Y. Sumino *et.al.*, *Phys. Rev.* **D47** (1993) 56.
36. A. Hoang, A. Manohar, and I. Stewart, *Phys. Rev.* **D65** (2002) 014014, hep-ph/0107144.
37. S. Groote and O. Yakovlev, *Phys. Rev.* **D63** (2001) 074012, hep-ph/0008156.
38. A. Hoang and T. Teubner, *Phys. Rev.* **D60** (1999) 114027, hep-ph/9904468.
39. S. Dawson and L. Reina, *Phys. Rev.* **D59** (1999) 054012, hep-ph/9808443.
40. S. Dittmaier et al, *Phys. Lett.* **B441** (1998)383, hep-ph/9808433.
41. A. Juste and G. Merino, hep-ph/9910301; A. Gay, www.desy.de/ desch/higgs/stmalo/gay.ps.
42. H. Baer, S. Dawson, and L. Reina, *Phys. Rev.* **D61** (2000) 013002, hep-ph/9906419.
43. L. Reina and S. Dawson, *Phys. Rev. Lett.* **87** (2001) 201804, hep-ph/0107101; S. Dawson, L. Orr, L. Reina, and D. Wackeroth, hep-ph/0211438; W. Beenakker *et. al.*, *Nucl. Phys.* **B653** (2003) 151, hep-ph/0211352; W. Beenakker *et. al.*, *Phys. Rev. Lett.* **87** (2001) 201805, hep-ph/0107-81.
44. G. van Oldenborgh and J. Vermaseren, *Z. Phys.* **C46** (1990) 425.
45. U. Baur, S. Keller, and D. Wackeroth, *Phys. Rev.* **D59** (1999) 013002, hep-ph/9807417.
46. J. Bagger, TASI95, hep-ph/9604232, M. Dine, TASI96, hep-ph/9612389, S. Martin, in *Perspectives on Supersymmetry*, ed. G. Kane (World Scientific, Singapore, 1998) hep-ph/9709356, S. Dawson, TASI97,hep-ph/9712464
47. C. Hill and E. Simmons, hep-ph/0203079.
48. J. Gunion *et. al.*, The Higgs Hunters Guide, (Addison-Wesley, Menlo Park, 1990).
49. M. Sher, *Phys. Rep.* **179** (1989) 273.
50. J. Casas, J. Espinosa, and M. Quiros, *Phys. Lett.* **B342** (1995) 171, hep-ph/9409458; **B382** (1996) 374, hep-ph/9603227.
51. M. Luscher and P. Weisz, *Nucl. Phys.* **B318** (1989) 705; A. Hasenfratz *et. al.*, *Nucl. Phys.* **B317** (1989) 81.

52. J. Wess and J. Bagger, *Supersymmetry and Supergravity*, (Princeton University Press, Princeton, 1983).
53. M. Carena et al, *Nucl. Phys.* **B580** (2000) 29, hep-ph/0001002; R. J. Zhang, *Phys. Lett.* **B447** (1999) 89, hep-ph/9808299; R. Hempfling and H. Hoang, *Phys. Lett.* **B331** (1994) 99, hep-ph/9401219; S. Heinemeyer, W. Hollik, and G. Weiglein, *Phys. Rev.* **D58** (1998) 091701, hep-ph/9803277.
54. M. Machacek and M. Vaughn, *Nucl. Phys.* **B222** (1983) 83; C. Ford *et. al.*, *Nucl. Phys.* **B395** (1993) 17.
55. V. Barger, M. Berger, and P. Ohmann, *Phys. Rev.* **D49** (1994) 4908, hep-ph/9311269.
56. B. Abbott *et. al.*, *Phys. Rev. Lett.* **82** (1999) 4975, hep-ex/9902028; R. Demina *et. al.*, *Phys. Rev.* **D62** (2000) 035011, hep-ex/9910275.
57. T. Affolder, *Phys. Rev. Lett.* **84** (2000)5704, hep-ex/9910049; *Phys. Rev. Lett.* **84** (2000) 5273, hep-ex/9912018.
58. G. Burdman, K. Land, and T. Rador, *Phys. Lett.* **B514** (2001) 41, hep-ph/0012073.
59. E. Simmons, hep-ph/0211335.